

University of Louisville

ThinkIR: The University of Louisville's Institutional Repository

Electronic Theses and Dissertations

5-2019

A study on ultrasonic energy assisted metal processing : its correelction with microstructure and properties, and its application to additive manufacturing.

Anagh Deshpande
University of Louisville

Follow this and additional works at: <https://ir.library.louisville.edu/etd>



Part of the [Manufacturing Commons](#), [Metallurgy Commons](#), and the [Other Materials Science and Engineering Commons](#)

Recommended Citation

Deshpande, Anagh, "A study on ultrasonic energy assisted metal processing : its correelction with microstructure and properties, and its application to additive manufacturing." (2019). *Electronic Theses and Dissertations*. Paper 3239.

<https://doi.org/10.18297/etd/3239>

This Doctoral Dissertation is brought to you for free and open access by ThinkIR: The University of Louisville's Institutional Repository. It has been accepted for inclusion in Electronic Theses and Dissertations by an authorized administrator of ThinkIR: The University of Louisville's Institutional Repository. This title appears here courtesy of the author, who has retained all other copyrights. For more information, please contact thinkir@louisville.edu.

A STUDY ON ULTRASONIC ENERGY ASSISTED METAL PROCESSING:
ITS CORRELATION WITH MICROSTRUCTURE AND PROPERTIES, AND ITS
APPLICATION TO ADDITIVE MANUFACTURING

By

Anagh Deshpande

A Dissertation

Submitted to the Faculty of the
J.B. Speed School of Engineering of the University of Louisville
in Fulfillment of the Requirements
for the Degree of

Doctor of Philosophy
in Mechanical Engineering

Department of Mechanical Engineering
University of Louisville
Louisville, Kentucky, United States

May 2019

Copyright by Anagh Deshpande

May 2019

All rights reserved

A STUDY ON ULTRASONIC ENERGY ASSISTED METAL PROCESSING:
ITS CORRELATION WITH MICROSTRUCTURE AND PROPERTIES, AND ITS
APPLICATION TO ADDITIVE MANUFACTURING

By

Anagh Deshpande

A Dissertation Approved on

February 12, 2019

by the following Dissertation Committee

.....
Dr. Keng Hsu
Dissertation Chairman

.....
Dr. Sundar Atre
Dissertation Member

.....
Dr. Thomas Berfield
Dissertation Member

.....
Dr. Kevin Chou
Dissertation Member

DEDICATION

This dissertation is dedicated to my parents

Trilochan Deshpande

and

Leenata Deshpande

for their invaluable support and encouragement.

ACKNOWLEDGEMENTS

First and foremost, I would like to thank my advisor, Dr. Keng Hsu. This would not have been possible without his support, guidance and motivation. I cherish every discussion I have had with him over the years. He has been a great role model not only as an advisor and a researcher but also as a kind and considerate human being. His exemplary leadership and vision have motivated me throughout my journey as a PhD student.

I would also like to thank my PhD committee members, Dr. Sundar Atre, Dr. Thomas Berfield and Dr. Kevin Chou for taking time out of their busy schedule and providing constructive criticism for my research. I would like to extend my gratitude to Dr. Sundar Atre and Dr. Kunal Kate for their help and support during the transition to University of Louisville. I would like to thank Dr. Sundar Atre also for his invaluable guidance and advice.

I greatly appreciate Dr. Jacek Jasinski at the Conn Center for Renewable Energy for his insights and help with TEM. I would like to acknowledge the Electron Microscopy Center at University of Kentucky and the staff there, Dr. Nicolas Briot, Dr. Azin Akbari and Dr. Dali Qian, for their help with TEM sample preparation and also the Rapid Prototyping Center (RPC) at University of Louisville for their support with the Selective Laser Melting equipment in the facility.

I take this opportunity to thank my lab mates and colleagues Dr. Alireza Tofangchi, Pu Han, Sihan Zhang, Julio Izquierdo, Adithya Iyengar, Bradley Sims, Paramjot Singh, Dr.

Subrata Deb Nath, Dr. Harish Irrinki, Bhushan Bandiwdekar, Nirupama Warriar and Chang Woo Gal for their help and support throughout my time at University of Louisville.

I would like to thank my parents, Trilochan Deshpande and Leenata Deshpande, for their love and support. My elder brother Ojas Deshpande and his wife Amruta, my cousins Parag Deshpande and his wife Radhika, and Parimal Deshpande and his wife Rachana have given me constant encouragement. Last but not the least, I would like to thank my friends Poorva Shelke, Aditi Mitkar, Harshal Kasat and Vamsi Krishna for supporting me throughout this journey.

ABSTRACT

A STUDY ON ULTRASONIC ENERGY ASSISTED METAL PROCESSING, ITS CORRELATION WITH MICROSTRUCTURE AND PROPERTIES, AND ITS APPLICATION TO ADDITIVE MANUFACTURING

Anagh Deshpande

February 12, 2019

Additive manufacturing or 3d printing is the process of constructing a 3-dimensional object layer-by-layer. This additive approach to manufacturing has enabled fabrication of complex components directly from a computer model (or a CAD model). The process has now matured from its earlier version of being a rapid prototyping tool to a technology that can fabricate service-ready components. Development of low-cost polymer additive manufacturing printers enabled by open source Fused Deposition Modeling (FDM) printers and printers of other technologies like SLA and binder jetting has made polymer additive manufacturing accessible and affordable. But the metal additive manufacturing technologies are still expensive in terms of initial system cost and operating costs.

With this motivation, this dissertation aims to develop and study a novel metal additive manufacturing approach called Acoustoplastic Metal Direct-Write (AMD) that promises to make metal additive manufacturing accessible and affordable. The process is a voxel based additive manufacturing approach which uses ultrasonic energy to manipulate and deposit material. This dissertation demonstrates that the process can fabricate near-net shape metal components in ambient conditions.

This dissertation investigates two key phenomenon that govern the process. The first phenomenon investigated is ultrasonic/acoustic softening. It is the reduction in yield stress of the metals when being deformed under simultaneous application of ultrasonic energy. A detailed analysis of the stress and microstructure evolution during ultrasonic assisted deformation has been presented in this dissertation. Crystal plasticity model modified on the basis of microstructure analysis has been developed to predict the stress evolution.

The 2nd phenomenon investigated is ultrasonic energy assisted diffusion that enables the bonding of voxels during the AMD process. High resolution Transmission Electron Microscopy (HRTEM) and Energy Dispersive Spectroscopy (EDS) analysis has been used to quantify this phenomenon and also distinguish the process mechanics from other foil or sheet based ultrasonic joining processes.

TABLE OF CONTENTS

ACKNOWLEDGEMENTS	iv
ABSTRACT	vi
LIST OF TABLES	xii
LIST OF FIGURES	xiii
CHAPTER 1	1
1 INTRODUCTION	1
Chapter 2	8
2 INTRODUCTION TO ACOUSTOPLASTIC METAL DIRECT-WRITE (AMD) PROCESS	8
2.1 Introduction	8
2.2 Methodology	9
2.2.1 Apparatus	9
2.2.2 Process sequence.....	10
2.2.3 Multi-material printing.....	11
2.3 Results	11
2.3.1 Solid state metal printing	11
2.3.2 Multi-material printing.....	14
2.3.3 Process physics	15

2.4	Conclusion.....	16
Chapter 3.....		17
3	ACOUSTIC/ULTRASONIC SOFTENING AND ITS EFFECTS ON STRESS AND MICROSTRUCTURE EVOLUTION DURING DEFORMATION OF ALUMINUM..	17
3.1	Introduction	17
3.2	Kocks-mecking plasticity model.....	19
3.2.1	Kocks-Mecking model for crystal plasticity.....	19
3.2.2	Modification to K-M model to account for acoustic softening.....	22
3.3	EXPERIMENTAL METHODS.....	23
3.3.1	Apparatus	23
3.3.2	Uniaxial compression test.....	24
3.3.3	Microstructure characterization using EBSD	24
3.3.4	Sample preparation for TEM analysis	25
3.4	Results and discussion.....	25
3.4.1	Uniaxial compression test.....	25
3.4.2	Microstructure characterization using EBSD	26
3.4.3	Microstructure characterization using TEM.....	28
3.4.4	Reasons for using K-M model	29
3.4.5	Stress evolution modeling using K-M model	30
3.5	Conclusions	34

Chapter 4.....	36
4 MICROSTRUCTURE EVOLUTION OF FCC METALS DURING ULTRASONIC ENERGY ASSISTED DEFORMATION	36
4.1 Introduction	36
4.2 Experimental methods.....	38
4.2.1 Apparatus	38
4.2.2 Sample preparation for microstructural analysis	39
4.2.3 Sample preparation for TEM analysis	39
4.3 Results and discussion.....	40
4.3.1 Microstructural analysis of copper.....	40
4.4 Conclusion.....	52
Chapter 5.....	53
5 IN-PROCESS MICROSTRUCTURE TUNING IN SOLID-STATE AMBIENT CONDITION METAL DIRECT MANUFACTURING	53
5.1 Introduction	53
5.2 Experimental methods.....	55
5.2.1 Sample preparation for ebsd	55
5.2.2 Microhardness measurement	55
5.3 Results and discussion.....	56
5.3.1 Microstructure evolution during AMD process.....	56

5.3.2	Microstructure using SLM process and its comparison with AMD process	61
5.4	Conclusion.....	63
Chapter 6.....		65
6	ANALYSIS OF ULTRASONIC ENERGY ASSISTED DIFFUSION.....	65
6.1	Introduction	65
6.2	Experimental methods.....	67
6.2.1	Sample preparation for tem.....	67
6.3	Results and discussion.....	69
6.3.1	Microstructure at the interface	69
6.3.2	Analysis of diffusion.....	71
6.3.3	Estimation of effective inter-diffusivity coefficient	73
6.4	Conclusion.....	78
Chapter 7.....		79
7	CONCLUSION AND FUTURE WORK	79
7.1	Conclusion.....	79
7.2	Future work	81
REFERENCES		83
CURRICULUM VITAE.....		90

LIST OF TABLES

Table 3-1. Values of strain rate and acoustic energy density for each experiment run	24
Table 3-2. Table showing values of various constants used in modeling.....	33
Table 6-1. EDS quantification result in the amorphous region at the Al-Ni interface.	70

LIST OF FIGURES

Figure 1-1. Schematic of the topics tackled in this dissertation.	4
Figure 2-1. Apparatus for AMD process.	9
Figure 2-2. SEM images of an aluminum sample after 2 printing 2-layers.....	11
Figure 2-3. (a)-(d) An “L” shaped object printed on produced using Acoustoplastic Metal Direct-write as a stand-alone 3D printing process.	12
Figure 2-4. A “tensile-test” style specimen constructed using hybrid AMD-milling process.	13
Figure 2-5. Preliminary X-ray microtomography scans at the mid-sections of the sample.	13
Figure 2-6. Tensile testing results of the I-shaped sample printed using hybrid additive-subtractive mode of the AMD process.....	14
Figure 2-7. An optical image of a multi-material Al6061 and copper sample printed using AMD.	15
Figure 3-1. Schematic showing the experimental setup for the uniaxial compression tests.	23
Figure 3-2. Stress versus strain curves for different US energy densities and strain rates.	26
Figure 3-3. Color coded orientation maps for all experimental runs shown in Table 1. ..	27
Figure 3-4. Grain size variation with acoustic energy density and strain rate.	27

Figure 3-5. Bright field TEM image of the after-deformation microstructure of pure aluminum wire compressed under simultaneous application of acoustic energy of 493.61 J/m³ and strain rate of 9.54/s deformed to a strain of 29

Figure 3-6. Pole figures for all experimental runs in Table 1..... 30

Figure 3-7. Dislocation density evolution for three different acoustic energy densities. . 32

Figure 3-8. Experimental and predicted stress versus strain curves for all acoustic energy densities and strain rates. 34

Figure 4-1. EBSD map of a) Undeformed copper wire, b) copper wire deformed without any ultrasonic energy assistance, c) copper wire deformed with 500 J/m³ ultrasonic energy density, copper wire deformed with 710 J/m³ ultrasonic energy density and d) copper wire deformed with 710 J/m³ ultrasonic energy density to a higher compressive strain of 0.75. High angle grain boundaries are highlighted by thick black lines while low angle grain boundaries (or subgrain boundaries) are highlighted by thin blue lines. A1 represents the direction of compression..... 41

Figure 4-2. Grain orientation spread (GOS) map of a) copper wire deformed without any ultrasonic energy assistance, b) copper wire deformed with 500 J/m³ ultrasonic energy density, c) copper wire deformed with 710 J/m³ ultrasonic energy density and d) copper wire deformed with 710 J/m³ ultrasonic energy density to a higher compressive strain of 0.75. The blue grains have average GOS between 0-1.5, green ones have average GOS between 1.5-5 and yellow ones have average GOS between 5-100. 42

Figure 4-3. TEM bright field images of copper sample after deformation under simultaneous application of ultrasonic energy (US energy density= 500 J/m³. a) Flattened

grain structure after deformation, b) Recrystallized grain marked by red arrow and c) Subgrain boundaries formed in the vicinity of a primary grain boundary..... 43

Figure 4-4. Misorientation angle versus area fraction histogram for- a) Copper and aluminum deformed under the presence of same ultrasonic energy density level and b) undeformed copper wire, copper deformed without ultrasonic energy, copper deformed in the presence of ultrasonic energy density of 500 J/m³, 710 J/m³ and copper deformed in the presence of ultrasonic energy density of 710J/m³ to a higher strain..... 45

Figure 4-5. Inverse pole figure maps of a) Undeformed Al6061 wires, b) Al6061 wire deformed under the presence of ultrasonic energy density of 150 J/m³ and c) Al6061 wire deformed under the presence of ultrasonic energy density of 215 J/m³, b) and c) both compressed to a strain of 0.75. High angle grain boundaries are highlighted by thick black lines while low angle grain boundaries (or subgrain boundaries) are highlighted by thin blue lines. A1 represents the direction of compression. 47

Figure 4-6. Grain orientation spread (GOS) map of- a) Al6061 wire deformed with 150 J/m³ ultrasonic energy density and b) Al6061 wire deformed with 215 J/m³. The blue grains have average GOS between 0-1.5, green ones have average GOS between 1.5-5 and yellow ones have average GOS between 5-100..... 47

Figure 4-7. a) STEM image of Al6061 wire deformed with 210 J/m³ ultrasonic energy density, b) bright field TEM image of the same sample showing precipitates and, c) bright field TEM image showing subgrain boundary..... 48

Figure 4-8. EDS map of the Al6061 sample deformed with 210 J/m³ ultrasonic energy density. Table show the quantitative EDS point analysis for the 2 precipitates shown in the electron image. 49

Figure 4-9. Misorientation angle versus area fraction histogram for- a) undeformed Al6061 wire, Al6061 wire deformed under ultrasonic energy density of 150 J/m³ and 215 J/m³, b) Aluminum and Al6061 deformed under similar conditions of ultrasonic energy density.51

Figure 5-1. Figure showing an example of indentation created during the Vickers microhardness test..... 56

Figure 5-2. 3-layer sample fabricated using AMD and IPF images for each of the three layers. 58

Figure 5-3. Misorientation data for 3 layers of a sample fabricated using AMD. 59

Figure 5-4. EBSD micrograph taken at the interface between first layer and the substrate. 60

Figure 5-5. Figure shows the hardness variation across 3 layers in a sample fabricated using AMD. 60

Figure 5-6. SEM images of a IN718 sample printed using SLM process showing the formation of dendritic phases..... 61

Figure 5-7. Figure shows the dendritic structure formed in AlSi10Mg sample printed using SLM process. 62

Figure 5-8. a) EBSD map of single track of IN718 printed using SLM process, b) EBSD map of IN718 sample printed using SLM process..... 63

Figure 6-1. SEM images taken during the lift out of a thin electron transparent lamella of the Al-Ni interface region. 68

Figure 6-2. TEM bright field image of the Al-Ni interface. 69

Figure 6-3. EDS map of the Al-Ni interface showing presence of oxygen content at the interface..... 70

Figure 6-4. HRTEM image of the region with high defect density near the Al-Ni interface.	71
Figure 6-5. a) STEM of the bonded Al-Ni interface, b) Result of EDS line scan at the interface showing atomic percentage of each constituent versus distance.	72
Figure 6-6. Graph showing the width of inter diffusion zone for different levels of ultrasonic energy densities.....	73
Figure 6-7. Graph of inter-diffusion coefficient between aluminum and nickel as a function of Ni atomic percentage for energy density of 310 J/m^3	74
Figure 6-8. a) High speed IR camera snap shot of the instant at which maximum temperature rise is observed during the process, b) Temperature evolution at the interface versus time.	76
Figure 6-9. HRTEM image of the Al-Ni interface.	77

CHAPTER 1

INTRODUCTION

Since the 1970s, the process of constructing a 3-dimensional object “additively” layer by layer has evolved from a rapid prototyping tool for concept visualization to now additive manufacturing technologies promising end-user engineering application in the near future. It is developing in the direction to not only revolutionize the manufacturing industry, but to redefine fundamentally how things are made. The implication of this transition is immense: it permeates conceivably every level of the human experience: aerospace, automobiles, bio-medical, military, electronics, consumer goods, foods, and personal products [1]. Currently, polymer additive manufacturing, or 3D printing, is accessible and affordable. Systems from \$200 Do-it-Yourself kits to large production system costing more than \$500,000 can be readily acquired. This trend is expected to continue in the near future [2]. Solid metal 3D printing, however, does not see the same development trajectory because of the innate safety concerns and technology and operation costs of existing metal technologies capable of producing solid metal components with densities greater than 95% [3] [4].

Current metal additive manufacturing processes include indirect methods such as Binder Jet processes and Selective Laser Sintering, and direct methods such as Selective Laser Melting, Electron Beam Melting, Laser Engineered Net Shaping, and more recently cold spray [5]. Indirect methods require post-processing such as Hot Isostatic Pressing to produce parts of density greater than 90% while direct methods can typically produce parts

with more than 90% density with optimized process parameters. In indirect methods, metal powders are either partially solid-state sintered together or a low-melting point binder is used to bind metal particles together to produce a preform. Post-processing operations such as binder removal, sintering or liquid metal infiltration are used to obtain greater than 90% build density [3]. The process of Ultrasonic Consolidation (or Ultrasonic Additive Manufacturing, UC/UAM) was introduced by researchers as a hybrid additive-subtractive process where sheets (or strips) of metal foils are first ultrasonically welded into a stack using a roller sonotrode. A cutting operation (often end-milling) is then used to shape the metal stack into the desired layer shape [6]. By alternating between these welding and cutting processes, 3-dimensional objects are constructed. In UC, the 2D shape of layers is obtained by combining a tape or sheet welding process and the subsequent trimming of welded layer to the desired shape. This process is capable of producing pure metal, alloy, and composite material parts with the use of high power ultrasonics and high mechanical loads [7] [8].

The powder-bed process has entered technology maturity, and is currently the most common metal 3D printing system for production of engineering components. Current systems of this process use thermal energy to melt and fuse material through manipulation of a melt pool created by laser or electron beam coupled into metal powder as heat. The resulting structures, morphology, and microstructures of printed materials depend highly on the thermal-physical and heat-transfer processes during the micro-welding event [3] [5]. These processes use fine powders as the starting material which can pose health and safety concerns especially when reactive metal powders such as aluminum are used [4]. Because of the heat melt-fusion nature of this technology, the part building process takes place under

controlled environment of inert gases or vacuum to prevent excessive oxidation, beam scattering in the case of electron beam melting, and process hazards [9] [4]. Though high-quality metal parts can be produced, a typical powder bed metal system starts at \$200,000 with an approximately 800 cm³ build volume, without taking into account the ancillary equipment and facility required to safely handle and process metal powders [10]. For a system with a build volume practical for production of engineering structural components, half a million to a few millions worth of capital investment alone can be expected.

Although in early stages of development, there have been new processes introduced that can allow 3D printing of metals with greater than 95% density without thermal melt fusion. Hu et al demonstrated a meniscus confined 3D electrodeposition approach that is capable of producing microscale 3D copper features of more than 99% density [11]. This process showed potential in high-resolution direct printing of fine features with the potential issues of slow deposition rate and limited number of materials available. A number of researchers demonstrated the ability to deposit metals such as copper and silver using a laser-induced chemical reduction process and the ability to have high spatial selectivity and increasing deposition rates [12] [13]. These chemical reduction and deposition based approaches, however, have common issues in spatial deposition selectivity as the deposited structure increases in height. The process of gas metal arc weld metal 3D printing is a recently developed inexpensive way of building metal components using an automated articulating welding toolhead [14] [15] [16]. This essentially metal welding process allows for a direct writing method where materials are used only when needed (as compared with the powder-bed approach where powder is dispersed across the entire build space at each layer). It is, however, based on melt-fusion of metals and as a result the thermal physical and thermal

mechanical property are similar to weld joints and to parts made using powder-bed melt fusion processes.

In contrast to these current additive manufacturing processes, the process investigated in this dissertation, Acoustoplastic Metal Direct-Write (AMD), is a solid-state acoustic energy based metal additive manufacturing process that can produce near net-shape metal components. This process can be implemented as a near-net shape process or a hybrid additive-subtractive process to produce solid metal parts of 95.3% to 99.5% density. The process prospectively can enable desktop 3d printers that can make metal 3d printing cost effective, scalable and accessible. The process and its fundamental physics are explored in this dissertation.

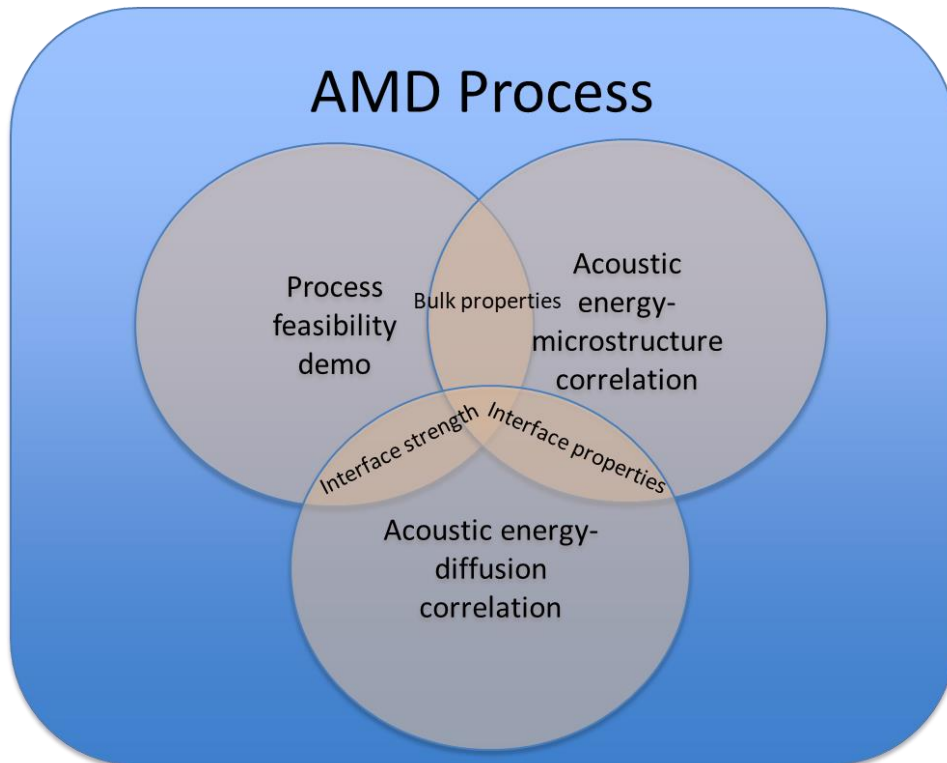


Figure 1-1. Schematic of the topics tackled in this dissertation.

A schematic of the topics tackled in this dissertation is shown in Figure 1-1 and the objectives of this dissertation are listed below:

1) The first objective is to develop and study an acoustic energy (or ultrasonic energy) based metal additive manufacturing process, called Acousticplastic Metal Direct-write (AMD), that can produce near net-shape metal components.

The development of this process will lead to a technology that will compliment current additive manufacturing technologies by making metal additive manufacturing affordable and scalable. Potentially, the process also could provide an alternative to additive manufacturing of materials like aluminum and aluminum alloys which are difficult to manufacture using powder bed fusion processes. Being a solid-state process, the process enables multi-material additive manufacturing of materials with disparate temperatures, and metals and polymers. Chapter 2 of this dissertation provides introduction and demonstration of the process along with an introduction to the physical phenomenon of ultrasonic/acoustic softening and ultrasonic energy assisted mass transport/diffusion that govern the process.

2) The second objective of this dissertation is to study the interaction of ultrasonic energy with metals and analyze its effects on evolution of stress, microstructure and the interfacial bond during deformation and deposition of one voxel of material during the AMD process.

The insight obtained in this work advances understanding of parameter-microstructure-property correlation not only for the AMD process but also for other manufacturing processes such as wire bonding, ultrasonic consolidation, and ultrasound assisted

incremental forming. It can also enable a new array of ultrasonic-vibration energy-assisted advanced manufacturing processes and augment the existing industrial processes.

To investigate the effect of ultrasonic energy on stress and microstructure evolution, in Chapter 3, characterization of microstructure using Electron Backscatter Diffraction (EBSD) analysis of the aluminium samples (fine wires) after compression under simultaneous application of ultrasonic energy has been carried out. A one-internal-variable crystal plasticity model called the Kocks-Mecking model has been used to model the effect of simultaneous ultrasonic energy irradiation on stress evolution during compression.

In chapter 4, the effect of stacking fault energy on the microstructure evolution during ultrasonic energy assisted compression has been investigated using EBSD and TEM analysis of aluminum, copper and aluminum 6061 alloy. An analogy between the resulting microstructure post hot deformation and ultrasonic assisted deformation has been shown. A thorough analysis through a comparison between high stacking fault energy material (aluminum) and medium stacking fault energy material (copper) has been presented.

Chapter 5 presents a comparison of the microstructure evolution during the AMD process as subsequent layers are added versus the microstructure evolution during Selective Laser Melting (SLM) process. During the SLM process, the material experiences a phase change. The differences in the microstructure that arise due to difference in the processing route during the solid-state AMD process and SLM process are highlighted.

Chapter 6 delves in to the ultrasonic energy assisted mass transport. This mass transport allows the bonding of material in the AMD process. By bonding aluminum wires to nickel

substrates, followed by Transmission Electron Microscopy analysis of the interface between two materials, a detailed analysis of the process mechanism has been presented.

CHAPTER 2

INTRODUCTION TO ACOUSTOPLASTIC METAL DIRECT-WRITE (AMD) PROCESS

2.1 INTRODUCTION

In this chapter, the process Acoustoplastic Metal Direct-write (AMD) is introduced and demonstrated. The working principle of this process can be thought of as the combination of Wire Bonding and Fused Deposition Modeling (FDM): a solid metal filament is used as the starting material to form a 3 dimensional object via the metallurgical bonding between the filaments and layers. The solid metal filament is guided, shaped, and then metallurgically bonded to the substrate (or the previous layer) as well as the adjacent filaments voxel by voxel using a guide tool on a positioning system. The key characteristics of this process are that (1) the mechanical stress (and therefore mechanical energy input) required to “shape” the filament into the desired “track” geometry is drastically reduced ($< 50\%$) in the presence of applied acoustic energy as compared to the yield strength of the material, (2) the amount of mass transport across the inter-filament and inter-layer interfaces to form the metallurgical bonds observed is higher [17] than what Fick’s diffusion predicts under the observed conditions, and (3) the temperature rise of the AMD process is nearly negligible (5 degrees Celsius) [18] [19]. In the subsequent chapters of this dissertation, each of these characteristics of the process have been analyzed in detail.

This chapter provides a detailed description of the experimental setup of AMD process. AMD of pure aluminum and multi-material printing of copper and Al6061 alloy are also demonstrated in this chapter.

2.2 METHODOLOGY

2.2.1 APPARATUS

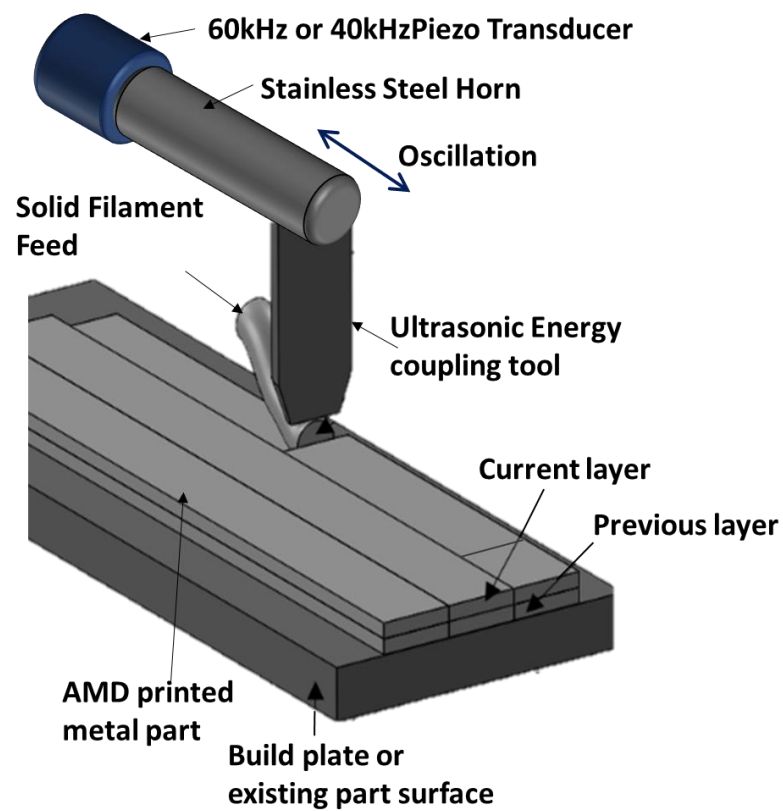


Figure 2-1. Apparatus for AMD process.

The apparatus has been shown in Figure 2-1. An X-Y-Z gantry based positioning system is used to manipulate a stainless-steel horn connected to a piezoelectric crystal oscillating at a frequency of 40 or 60 kHz. The ultrasonic energy supplied to the aluminum voxel is

modulated through vibrational amplitude and time. At the end of the stainless-steel horn is a tungsten carbide tool (a 3mm-dia. cylindrical rod of tungsten carbide with a flat end of 800um x 800um) which guides and forms voxels from a fine filament. In addition to acoustic energy input modulation, the force with which the metal filament is pressed onto the substrate/existing layer can also be controlled.

2.2.2 PROCESS SEQUENCE

The process begins by bringing the tool guiding the filament to the desired voxel location and holding the filament in place with nominal pressure. Once positioned, the aluminum filament is supplied with ultrasonic energy through the tool. The combination of force applied by the tool and the irradiation of acoustic energy allows the section of the filament defined by the tool-filament contact to form and to fuse onto the substrate/existing layer, forming the voxel. During voxel formation, the tool moves towards the substrate/existing surface, compressing and shaping the aluminum filament from a circular cross-section into a slab of aluminum. This process repeats as the tool moves along the axis of the metal filament until the desired “track” is completed. Each voxel overlaps with the previous and the following voxels and with those in the adjacent tracks. This process then repeats for each track and for each layer. Figure 2-2 shows SEM images of an aluminum sample after 2 layers have been printed. In the current implementation of the AMD process, at the end of each track, the metal filament is manually sheared off to allow the tool to translate to the first voxel in the following track.

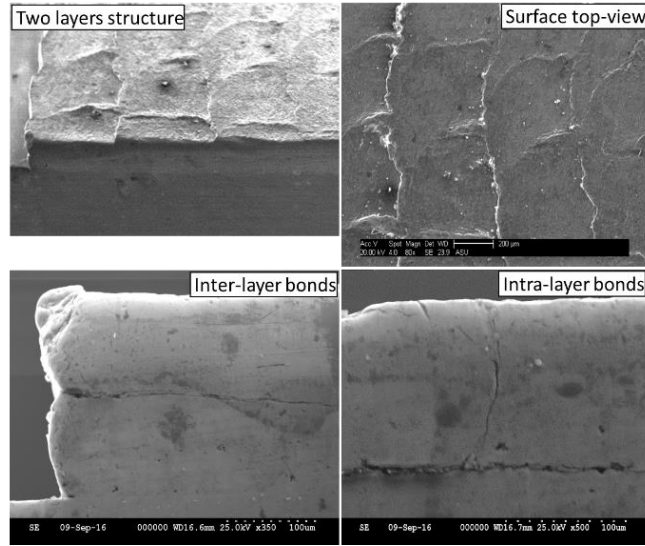


Figure 2-2. SEM images of an aluminum sample after 2 printing 2-layers.

2.2.3 MULTI-MATERIAL PRINTING

To demonstrate the capability of AMD process in printing multi-material components, a sample with two different metals, copper and Al6061, was printed. To do this, first a track of Al6061 was deposited on the substrate. After this, a track of copper was deposited besides the Al6061 track. This process was repeated to form a layer of copper and Al6061 tracks. 2 such layers of Al6061 and copper tracks juxtaposed besides each other were printed to create a 3d multi-material slab.

2.3 RESULTS

2.3.1 SOLID STATE METAL PRINTING

An L-shaped 3D object and a tensile testing specimen were built following the procedure for AMD process described in the previous section. In the case of the L-shaped object, post-process of surface re-finish was used to remove features (less than 200 micro-meters) from the printing process. As shown in Figure 2-3(a) through (d), the object is 5mm long, 4mm wide, and approximately 1.5mm tall with a layer height of 125 microns.

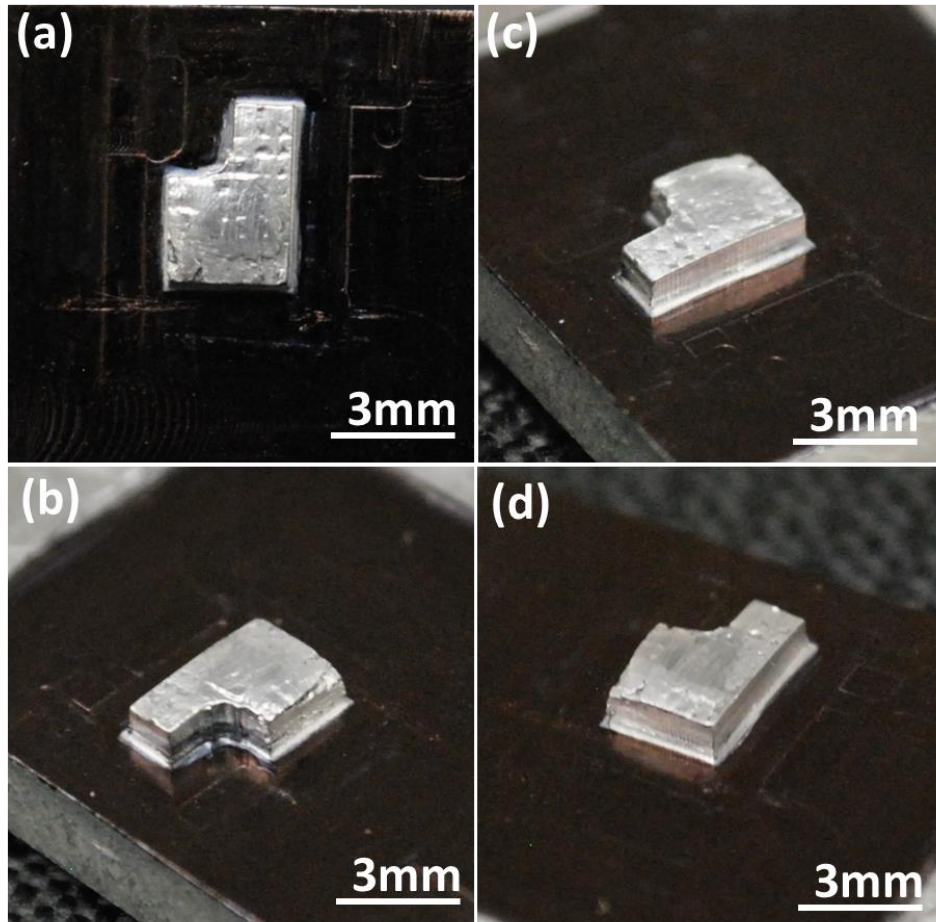


Figure 2-3. (a)-(d) An “L” shaped object printed on produced using Acoustoplastic Metal Direct-write as a stand-alone 3D printing process.

The hybrid additive-subtractive mode of the process was also demonstrated. A 16 layer-aluminum structure was printed and machined down to an I-shaped object as photographed and shown in Figure 2-4. Preliminary X-ray microtomography scans at the mid-section of the sample are shown in Figure 2-5. In the x-ray scans of the AMD printed sample, the inter-layer interfaces are discernable, while no inter-filament interfaces are observed. Density values were measured by calculating the porosity within the sample in each image using ImageJ software. Values of 95.3% to 99.5% are observed.

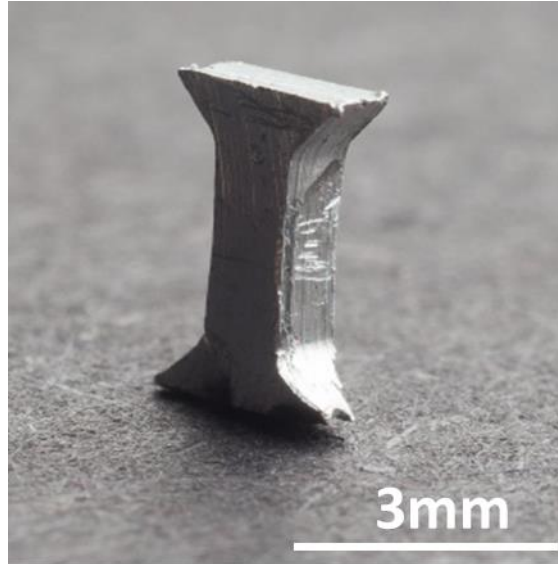


Figure 2-4. A “tensile-test” style specimen constructed using hybrid AMD-milling process.

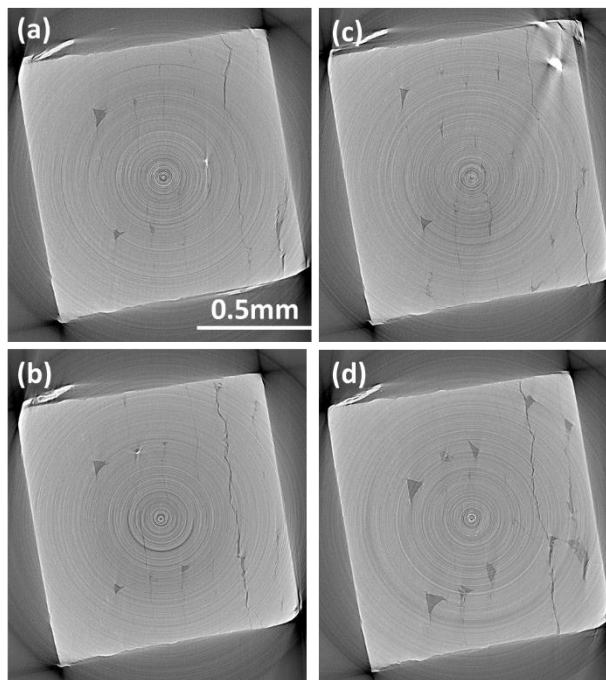


Figure 2-5. Preliminary X-ray microtomography scans at the mid-sections of the sample.

Tensile testing data is shown in Figure 2-6. The stress versus strain curve shows that the specimen went through a significant amount of plastic deformation before fracture. Ultimate tensile strength of the specimen is 88% of the bulk ultimate tensile test of pure aluminum. Reduction in the ultimate tensile strength can be attributed to the inter-filament porosity shown in Figure 2-5.

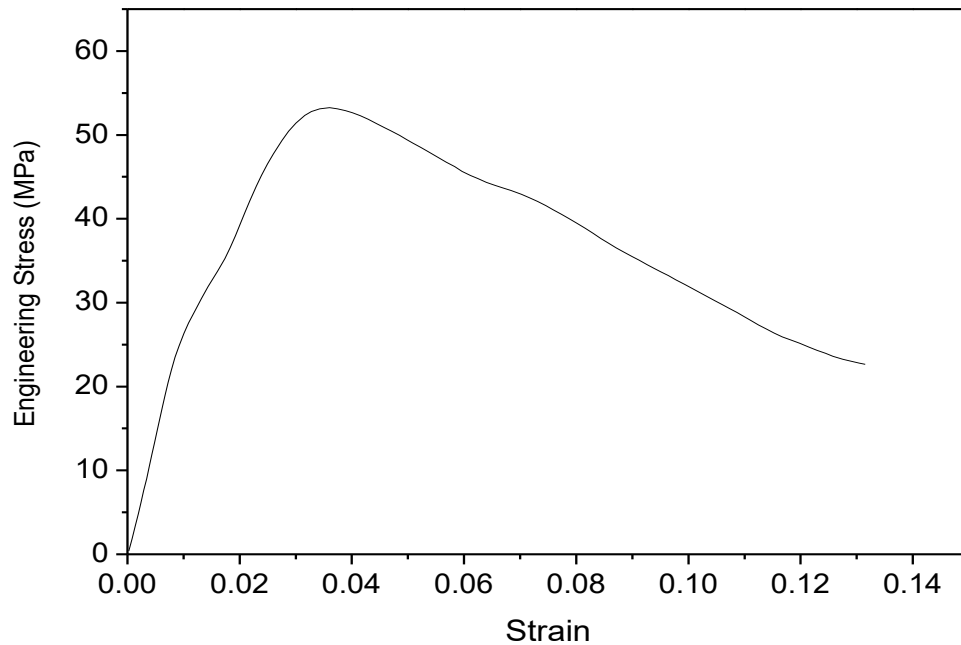


Figure 2-6. Tensile testing results of the I-shaped sample printed using hybrid additive-subtractive mode of the AMD process.

2.3.2 MULTI-MATERIAL PRINTING

An optical image of a multi-material Al6061 and copper sample printed using AMD is shown in Figure 2-7. The voxel-by-voxel deposition method used in AMD allows for printing of two different materials within the same layer. Also, since it is a solid-state process, materials with disparate melting temperatures can also be printed, which is typically not feasible using powder-bed fusion methods.

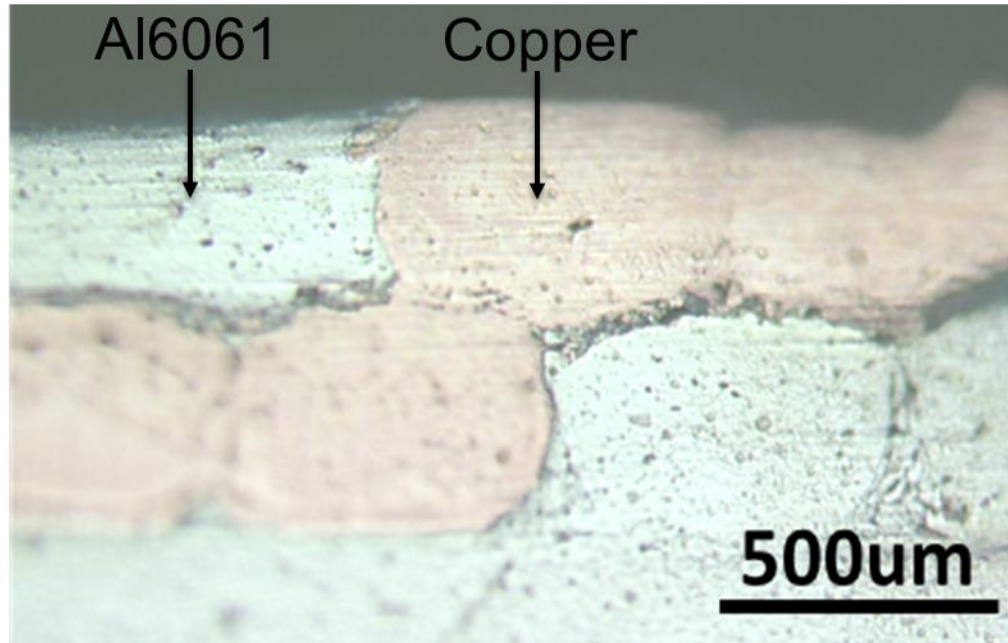


Figure 2-7. An optical image of a multi-material Al6061 and copper sample printed using AMD.

2.3.3 PROCESS PHYSICS

The physical phenomena that enable Acoustoplastic Metal Direct-write are attributed firstly to the well observed acoustic or ultrasonic softening of crystalline metals, and secondly to a mechanism that involves drastically increased mass transport at the crystal lattice level over large spatial domains (hundreds of nanometers) within a short amount of time (less than 1 second) [20]. During AMD process, the ultrasonic energy irradiated to the metal softens it allowing for the shaping of deposited voxel at stresses much lower than the yield stress of the metal. At the same time, the large scale mass transport allows for the solid state bonding of the voxel to the lower layer or the substrate.

The detailed analysis of the phenomenon of acoustic or ultrasonic softening and ultrasonic energy assisted mass transport/diffusion are described in the next 4 chapters of the dissertation.

2.4 CONCLUSION

In this chapter, the process Acoustoplastic Metal Direct-write is introduced wherein a solid metal filament is used to form 3D objects through a voxel-track-layer-bulk process under ambient conditions at room temperature. In the current state millimeter-scale aluminum objects have been printed and demonstrated. This process can be implemented as a near-net shape process or a hybrid additive-subtractive process to produce solid metal parts of 95.3% to 99.5% density. The chapter also gives an introduction of the two physical phenomenon of acoustic/ultrasonic softening and ultrasonic energy assisted diffusion/mass transport that govern the process. Further details of the two phenomenon have been described in the next chapters.

CHAPTER 3

ACOUSTIC/ULTRASONIC SOFTENING AND ITS EFFECTS ON STRESS AND MICROSTRUCTURE EVOLUTION DURING DEFORMATION OF ALUMINUM

3.1 INTRODUCTION

Acoustic softening has been used to improve several manufacturing processes by taking advantage of the associated reduction in stresses required to achieve plastic deformation. One of the first explanations to this observed reduction in yield stress of a metal during deformation due to simultaneous application of acoustic energy was presented by Langenecker in 1966 [21]. This reduction in yield stress of metals was attributed to the preferential absorption of acoustic energy at the lattice defects, more specifically dislocations, resulting in a reduction in the stress required to move the dislocations [21] [22].

Tang et al. used longitudinal-torsional composite ultrasonic vibration for titanium wire drawing and observed a reduction in drawing force and better surface finish [23]. Abdullah et al. used longitudinal ultrasonic vibrations to reduce the axial forming forces and improve the surface quality during indentation formation of tubes [24]. Similarly, ultrasonic vibrations were shown to increase formability and decrease forming forces during the forming of AA1050 sheets by Amini et al [25]. More recently, ultrasonic vibration assistance was shown to improve weld formation in friction stir welding by Zhong et al [26]. In the hybrid additive-subtractive manufacturing process called Ultrasonic Consolidation, acoustic softening has been observed and shown to have significant effects

on the process parameters. Wire bonding is another process which uses acoustic softening to deform metal wires along with an athermal ultrasonic assisted diffusion phenomenon to bond the wires to a substrate [22] [27] [28]. Considering the applications of acoustic softening to several manufacturing processes, understanding of the effects of acoustic softening on metals, particularly on their microstructure which affects the eventual material properties, becomes important.

Several attempts have been made to model the behavior of metals during deformation under the influence of acoustic energy irradiation. Rusinko modified the synthetic theory of irreversible deformation to develop an analytical model of acoustic softening and residual hardening by introducing a new term called ultrasonic defect density [29]. Siddiq and Sayed modified the porous plasticity model to account for the acoustic softening effects during ultrasonic manufacturing processes [30]. Yao et al. modified the single crystal plasticity frame work to model acoustic softening and residual hardening during the upsetting experiments [31]. However, these models do not provide a full explanation of the phenomenon of acoustic softening, especially in regards to microstructure evolution during the deformation process with simultaneous application of acoustic energy. The study of this microstructure evolution can provide a significant insight about the phenomenon which can further help in the development of a constitutive model that accurately models the stress evolution.

In this chapter, characterization of microstructure using Electron Backscatter Diffraction (EBSD) analysis of the aluminium samples (fine wires) after compression has been carried out. The microstructure characterization shows evidence of athermal dynamic recovery similar to that observed during hot deformation. A one-internal-variable crystal plasticity

model called the Kocks-Mecking model has been used to model the effect of simultaneous acoustic energy irradiation on stress evolution during compression. The model is similar to that used by Yao et al. [31], but several changes have been made to the model to account for athermal acoustic energy enabled dynamic recovery. Discrepancies in the results with those of Yao et al. have been highlighted and explanations have been provided for the same. The results are significant for processes like wire bonding in which a similar setup is used to deform and bond fine wires and also for manufacturing processes like ultrasonic assisted forming, wire drawing and consolidation which use the phenomenon of acoustic softening.

3.2 KOCKS-MECKING PLASTICITY MODEL

3.2.1 KOCKS-MECKING MODEL FOR CRYSTAL PLASTICITY-

During hot deformation, as material is strained, new dislocations are generated in the material resulting in a rise in the stress required for further deforming the material (strain hardening). At the same time, dislocations annihilate, or entangle into low energy arrays forming subgrain boundaries, due to climb of edge dislocations made possible by the increased mobility of atoms at higher temperatures and cross glide of screw dislocation. When the rate of dislocation annihilation equals the rate of generation, a steady state is reached and there is no further increase in the stress [32] [33] [34].

For higher temperatures and lower strain rates, the increased mobility of dislocations enables the annihilation to be higher. So, the steady state is reached at lower overall dislocation density resulting in larger subgrain sizes while for deformation at lower temperatures and faster strain rates, the generation of dislocations is faster due to which the steady state is reached at higher overall dislocation density and smaller subgrain size.

The Kocks-Mecking model relates the plastic strain rate $\dot{\gamma}^p$ to the shear stress τ through the kinetic equation given by [35] [36]-

$$\dot{\gamma}^p = \dot{\gamma}_o \exp\left(\frac{-\Delta G}{kT}\right) \quad (1)$$

$\dot{\gamma}_o$ is called the pre-exponential factor, and ΔG is the Gibbs free energy. Gibbs free energy is a function of the obstacle distribution. It is related to total free energy ΔF via the equation [35] [36]-

$$\Delta G = \Delta F \left(1 - \left(\frac{\tau}{\hat{\tau}}\right)^p\right)^q \quad (2)$$

p and q have values 3/4 and 4/3 respectively and $\Delta F = 0.5\mu b^3$ [36]. μ is the shear modulus and b is the burgers vector.

The KM model is based on a single internal variable $\hat{\tau}$ called mechanical threshold which depends on dislocation density ρ . The mechanical threshold is a demarcation between thermally activated flow and viscous glide; below the mechanical threshold, plastic flow is only due to thermal activation and above it due to rate sensitive viscous glide [37]. The relation between mechanical threshold $\hat{\tau}$ and ρ is given by [35] [38] [39]-

$$\hat{\tau} = \alpha\mu b\sqrt{\rho} \quad (3)$$

where, α is a numeric constant.

The evolution of dislocation density with plastic strain is controlled by two terms; 1) the dislocation storage term that causes athermal hardening and which is inversely proportional

to the average spacing between dislocations and hence directly proportional to $\sqrt{\rho}$, and
 2) the dislocation annihilation term which accounts for the dynamic recovery due to the cross-slip of screw dislocations and climb of edge dislocations and is proportional to ρ [38] [35] [40]. For a detailed derivation for each term, readers are referred to [38].

$$\frac{d\rho}{d\gamma^p} = \frac{d\rho^+}{d\gamma^p} + \frac{d\rho^-}{d\gamma^p} = k_1\sqrt{\rho} - k_2\rho \quad (4)$$

where γ^p is the resolved shear strain in the slip plane. The coefficient for the dynamic recovery term k_2 is given by the equation [35] [40]-

$$k_2 = k_{20} \left(\frac{\dot{\gamma}^p}{\dot{\gamma}_o^*} \right)^{-1/n} \quad (5)$$

where k_{20} is a numeric constant. k_2 is strain rate and temperature dependent. For low temperature range, n is inversely proportional to temperature T and $\dot{\gamma}_o^*$ is constant but for high temperature range, $\dot{\gamma}_o^*$ is given by Arrhenius equation [35] [41]

$$\dot{\gamma}_o^* = \dot{\gamma}_{o0}^* \exp\left(\frac{-Q_d}{kT}\right) \quad (6)$$

where Q_d is activation energy for self-diffusion or dislocation climb, k is the Boltzmann constant and T is the temperature. For high temperature range, n is constant between 3 and 5 [37] [38] [35]. The demarcation between low and high temperature range is usually 2/3 of the melting temperature [41].

Finally, to relate shear stresses and strains in a single crystal to macroscopic axial stresses and strains in polycrystalline materials, Taylor's factor is used.

$$M = \frac{\sigma}{\tau} = \frac{\gamma^p}{\varepsilon^p} \quad (7)$$

M is microstructure dependent. The evolution of M is assumed to be much slower than the evolution of dislocation density. Hence, M is assumed to be constant [35].

3.2.2 Modification to KM model to account for acoustic softening

The after-deformation microstructure of the aluminium samples deformed under the influence of acoustic energy shows evidence of strain rate and athermal acoustic energy dependent dynamic recovery analogous to that observed during hot deformation. The details about the microstructure characterization results have been discussed in Results and Discussion section. To account for this acoustic energy induced dynamic recovery, equation (4) for $\dot{\gamma}_o^*$ was modified as follows-

$$\dot{\gamma}_o^* = \dot{\gamma}_{oo}^* \exp\left(\frac{-Q_d \chi}{kTE}\right) \quad (8)$$

E is the energy density in J/m^3 given by $E = a^2 \omega^2 \rho_{Al}$, where a is the amplitude of vibration, ω is the frequency in rad/s and ρ_{Al} is the density of aluminium. χ is a constant with units J/m^3 . It can be thought of as the minimum amount of acoustic energy density required to achieve acoustic softening. Increase in the amount of acoustic energy density during deformation results in an increase in the value of k_2 which accounts for the increased dynamic recovery induced by acoustic energy.

3.3 EXPERIMENTAL METHODS

3.3.1 APPARATUS

Figure 3-1 shows the experimental apparatus for the uniaxial compression tests. A stainless-steel horn is connected to a piezo transducer which vibrates at a frequency of 60 kHz. The stainless-steel horn amplifies the vibrations of the piezo transducer. A tungsten carbide coupling tool is connected to the horn and a 300 micron pure aluminium wire (99.9%) is fed between the tool and a surface plate. The surface plate is kept on a load cell (not shown in Figure 3-1) to measure the forces exerted by the tool on the wire during uniaxial compression tests. Amplitude of acoustic vibration at the tip is measured using a Polytec vibrometer.

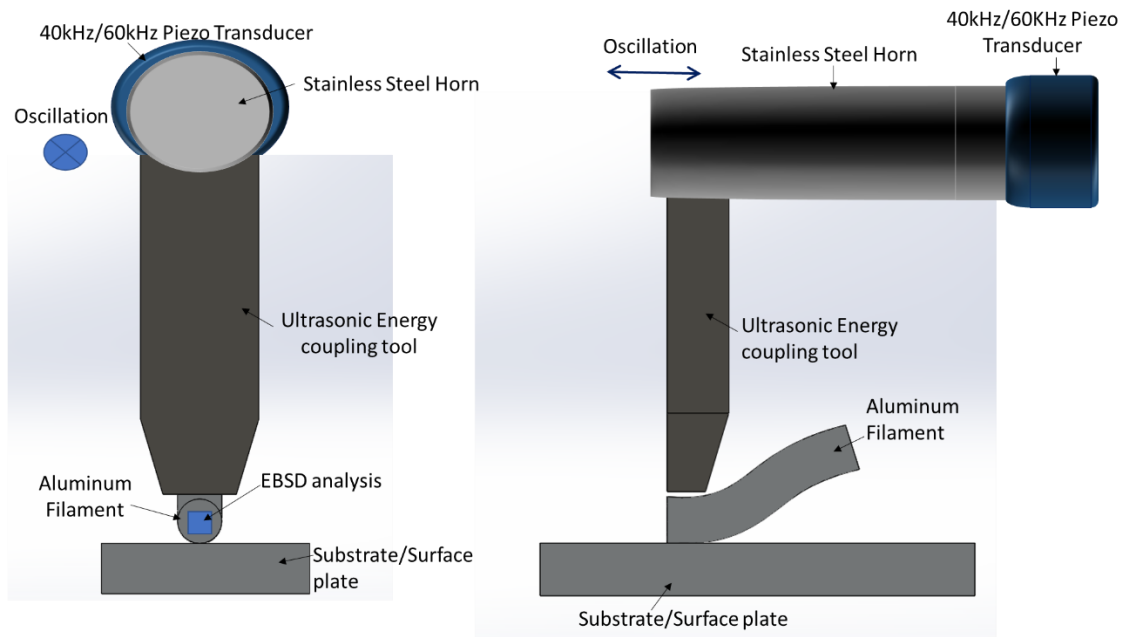


Figure 3-1. Schematic showing the experimental setup for the uniaxial compression tests.

3.3.2 UNIAXIAL COMPRESSION TEST

During the uniaxial compression tests, the tungsten carbide tool vibrates at 60 kHz frequency and at the same time compresses the 300 micron aluminium wire at a constant strain rate to a logarithmic strain of 1.1. Force exerted by the tool on the wire is recorded by the load cell. By deforming the filament at different strains, instantaneous area measurements were done to calculate the true stress. Several compression tests were conducted at different acoustic energy densities and strain rates to study the effect of acoustic energy density and strain rate on the stress and microstructure evolution. Table 3-1 provides the details about each experiment run. True Stress versus strain curves were plotted for experiment run.

Table 3-1. Values of strain rate and acoustic energy density for each experiment run

Sample number	strain rate (/s)	Energy density (J/m ³)
1	9.5	434.35
2	9.5	493.61
3	9.5	556.66
4	2.9	434.35
5	2.9	493.61
6	2.9	556.66

3.3.3 MICROSTRUCTURE CHARACTERIZATION USING EBSD

After deforming aluminium wires under the influence of acoustic energy, cross section of the wires was polished using standard metallographic procedure. Initially, the samples were polished starting with a 320 grit silicon carbide abrasive disc gradually progressing to 1200 grit silicon carbide abrasive disc. After this, further polishing was performed using 6 micron polycrystalline diamond particles followed by 1 micron polycrystalline diamond particles. A high-quality polish was achieved by polishing each sample with final 0.04

micron alumina slurry for 1 to 2 hours. Between each polishing step, samples were cleaned in an ultrasonic bath.

The polished samples were analyzed in a SEM equipped with an EBSD detector to obtain grain size and grain misorientation data.

3.3.4 SAMPLE PREPARATION FOR TEM ANALYSIS

To prepare samples for TEM analysis, a cross section of the sample along the length of the wire was cut. Same sample preparation method as described above was used to polish the samples. A FEI Helios Nanolab 660 dual beam Focused Ion Beam (FIB) was used to lift-out an electron transparent lamella of the sample. To do this, a protective platinum layer was deposited on the region of interest. Two trenches were milled on either side of the region of interest. The lamella (or region of interest) was then welded to a needle and separated from the bulk material. The lamella was transferred onto a copper half grid and further thinning was performed at low beam current. The lamellas so prepared were analyzed in a 200 kV FEI Tecnai F20 TEM/STEM equipped with an EDAX EDS detector.

3.4 RESULTS AND DISCUSSION

3.4.1 UNIAXIAL COMPRESSION TEST

Figure 3-2 shows the stress versus strain curves for a combination of experiments carried out for three different acoustic energy densities and two different compression strain rates as indicated in Table 3-1. It can be observed from the figure that, for any experimental condition, initially the stress increases indicating an increase in dislocation density. The slope of the curves decreases gradually, and the curves tend to become horizontal for higher values of strain indicating that the stress approaches a steady state and that the dislocation generation and annihilation are also tending to reach a balance.

For a particular strain rate, the steady state is reached at a lower value of stress for higher acoustic energy density providing an evidence for more softening with the use of higher acoustic energy densities. The effect of acoustic energy is more pronounced at higher strain rate. For a particular value of acoustic energy density, steady state is reached at a lower value of stress for lower strain rate indicating increased acoustic softening for lower strain rates. Hence, a strong strain dependence of the stress versus strain curve can be seen from Figure 3-2. This strong strain rate dependence is not in agreement with the results by Yao et al. [31] who observed that the strain rate has no effect on the amount of softening.

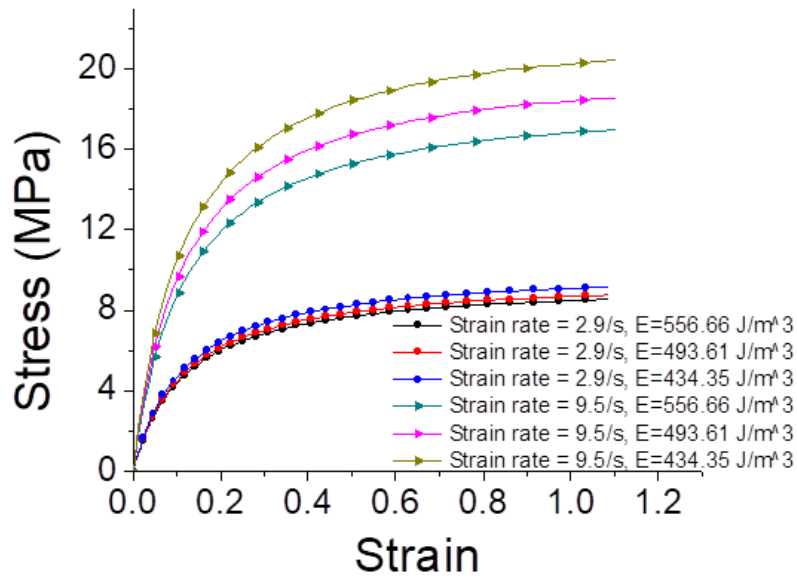


Figure 3-2. Stress versus strain curves for different US energy densities and strain rates.

3.4.2 MICROSTRUCTURE CHARACTERIZATION USING EBSD

Figure 3-3 a shows the color-coded orientation map of the cross-section of all the samples after compression under the influence of acoustic energy. The color-coded orientation maps show an increase in grain size with increase in the acoustic energy density used

during deformation. Also, with a decrease in strain rate, an increase in the grain size is observed. A more detailed graph of grain size variation with acoustic energy density and strain rate is shown in Figure 3-4.

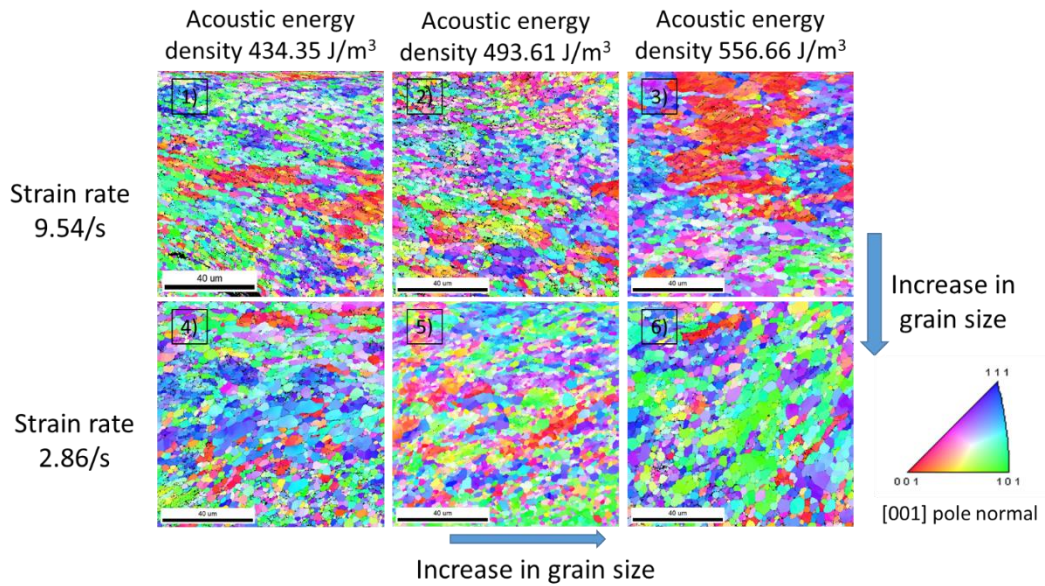


Figure 3-3. Color coded orientation maps for all experimental runs shown in Table 1.

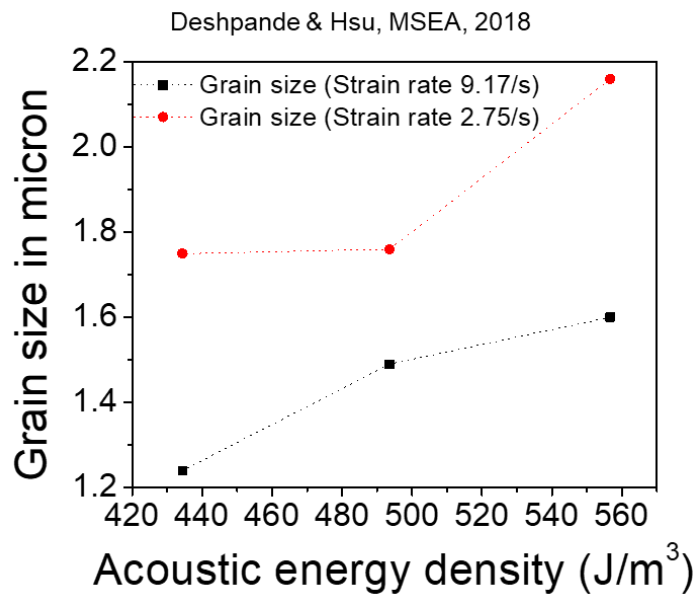


Figure 3-4. Grain size variation with acoustic energy density and strain rate.

The microstructure evolution during deformation under the influence of acoustic energy follows a similar trend to that during hot deformation. At higher acoustic energy densities, there is an acoustic energy enabled increase in dynamic recovery. This results in rapid dislocation annihilation. A similar increase in dynamic recovery is also observed during deformation with lower strain rates since the dislocations have more time to annihilate. Hence, the steady state between the generation and annihilation is reached at a lower overall dislocation density enabling larger subgrain size and also, lower flow stresses (Figure 3-2). On the other hand, at lower acoustic energy densities or higher strain rates, the dislocation annihilation is slower. So, the balance between generation and annihilation is achieved at higher overall dislocation density resulting in smaller grain sizes and, higher flow stresses (Figure 3-2).

3.4.3 MICROSTRUCTURE CHARACTERIZATION USING TEM

Figure 3-5 shows a bright field TEM image of the after-deformation microstructure of pure aluminum wire compressed under simultaneous application of acoustic energy of 493.61 J/m³ and strain rate of 9.54/s. The formation of subgrain boundaries by entangled dislocations is clearly evident and is labeled and marked. A very low dislocation density can be observed in the sample even though the sample is deformed to a compressive strain of 1.1.

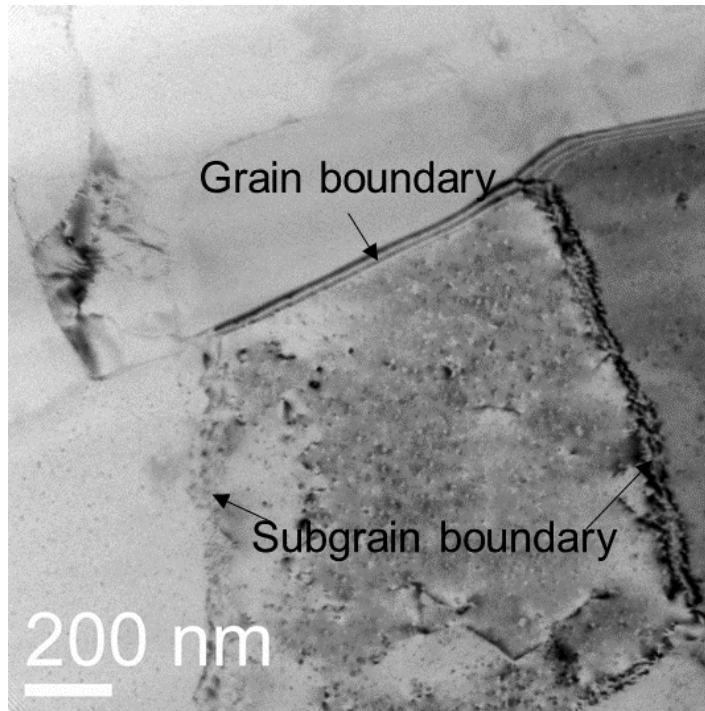


Figure 3-5. Bright field TEM image of the after-deformation microstructure of pure aluminum wire compressed under simultaneous application of acoustic energy of 493.61 J/m³ and strain rate of 9.54/s deformed to a strain of

3.4.4 REASONS FOR USING K-M MODEL

The observations in previous 2 sub-sections are the basic rationale behind using the Kocks-Mecking model for modeling the stress evolution. In KM model, the generation and annihilation of dislocations are governed by k_1 and k_2 respectively as indicated by equation (4). k_2 is the strain rate and temperature dependent term. Hence, to account for the acoustic energy enabled dynamic recovery, modifications were made to $\dot{\gamma}_o^*$ in equation (5), and equation (6) was replaced with equation (8). If higher acoustic energy density is used, the value of $\dot{\gamma}_o^*$ reduces. This increases value of k_2 and hence the rate of annihilation in the model.

In the pole figures shown in Figure 3-6, A1 is the direction of compression and A2 is the orthogonal direction. For all microstructures, $\langle 111 \rangle$ direction is preferentially aligned in the A1 direction. In aluminium which has a FCC structure, the $\langle 111 \rangle$ planes are the closed packed planes and hence the normal to these planes preferentially orients in the direction of deformation [42].

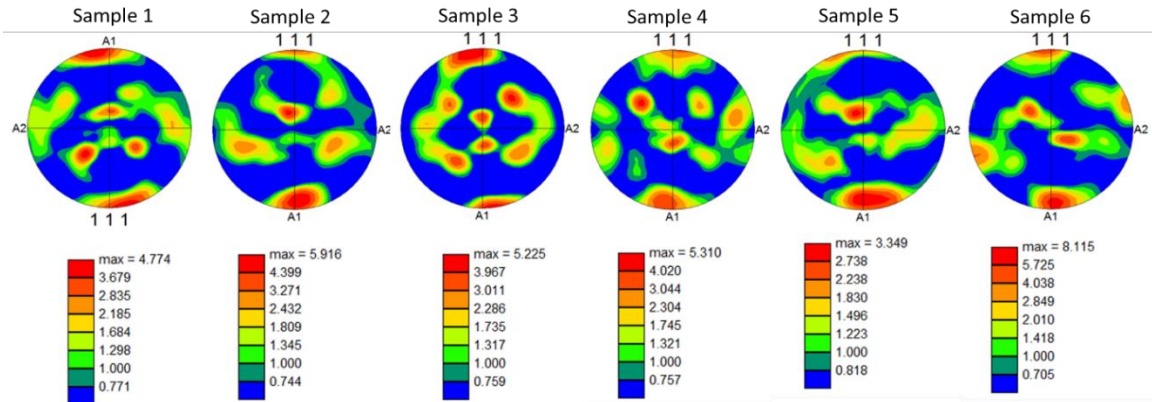


Figure 3-6. Pole figures for all experimental runs in Table 1.

3.4.5 STRESS EVOLUTION MODELING USING KM MODEL

To model the stress evolution during compression tests under the influence of acoustic energy, experimental data was used to find several parameters in the KM model. Table 3-2 shows the list of parameters used from references and the parameters identified using experimental data. Experimental data of one experimental run (US energy density=434.35 J/m³ and strain rate= 9.54/s) was used to predict evolution of dislocation density with strain. Figure 3-7 shows the graph of predicted dislocation evolution versus strain for three different acoustic energy densities. It can be seen from the graph that the dislocation density approaches a steady state for larger values of strain. As mentioned earlier, the steady state for dislocation density evolution is reached at a lower value of dislocation density for

higher acoustic energy densities. This predicted dislocation density evolution is very different from the predicted dislocation density evolution observed by Yao et al. In [31], the slope of the predicted dislocation density versus strain curve increases rapidly with strain indicating continuous hardening in the material with increase in strain. As a consequence of this, the slope of stress versus strain curve should also rapidly increase. But surprisingly, the slope of the stress-strain curve decreases with increase in strain [31]. This disparity in the predicted dislocation density evolution and stress evolution in [31] is phenomenologically counter intuitive.

Using curve fitting, the coefficient of the athermal dislocation generation term (k_1) and the coefficient of the strain rate and acoustic energy density dependent annihilation term (k_2) in equation 4, and exponent n in equation 5 were determined. Similarly, the coefficient k_2 for each acoustic energy density was determined. Using curve fitting, constants k_{20} in equation 5 and $\dot{\gamma}_{oo}^*$ and χ in equation 8 were determined.

These constants were used in the equations (1)-(8) to find stress values for increasing strain values. Using these stress values, stress versus strain curves were plotted for all experimental runs. Figure 3-8 shows the experimental and predicted curves for all acoustic energy densities and strain rates. It is clear from Figure 3-8 that for higher acoustic energy densities, the stress strain curve approaches a steady state value at lower stresses. This can be attributed to the balance between dislocation annihilation and generation being reached

at lower overall dislocation density due to the increased acoustic energy enabled dynamic recovery.

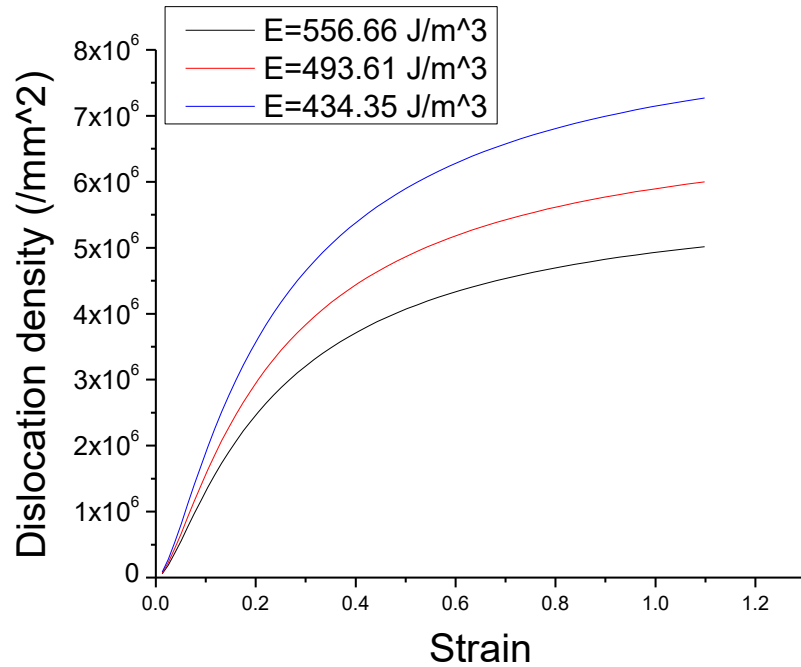


Figure 3-7. Dislocation density evolution for three different acoustic energy densities.

By comparing the experimental and predicted stress versus strain curves in Figure 3-8, it can be seen that for all curves, the predicted stress versus strain curves reach a steady state faster than the experimental curves. The slope of all predicted stress versus strain curves is almost zero for a strain of 1. This could be because the microstructure dependent value of Taylor factor M has been considered to be constant assuming that the evolution of dislocation density is much faster than the evolution of the microstructure. In reality, due to the slow evolution of microstructure, value of M changes causing a prediction of the steady state at lower values of strain. To eliminate this, modified KM models can be used to incorporate the changing value of M with microstructure evolution [35].

The KM model described and implemented assumes plasticity from the beginning of loading. In other words, the KM model does not accommodate yielding phenomenon. This is also the reason why a finite stress is predicted by the KM model for zero strain [35].

Table 3-2. Table showing values of various constants used in modeling

	Parameter	Value	Equation number	Reference
Parameters from reference	Pre-exponential factor, $\dot{\gamma}_o$ (/s)	10^6	(1)	[36]
	Shear modulus, μ (MPa)	26×10^3	(2), (3)	[31]
	Burgers vector, b (nm)	0.286	(3)	[31]
	Exponent in equation (2), p	3/4	(2)	[36]
	Exponent in equation (2), q	4/3	(2)	[36]
	Constant in equation (3), α	1/3	(3)	[43]
	Activation energy, Q_d (kJ/mol)	144	(6)	[44]
	Taylor factor, M	3.06	(7)	[36]
Experimentally determined parameters	Coefficient in equation (4), k_1	10779.5	(4)	
	Exponent in equation (5), n	3.4	(5)	
	Coefficient in equation (5), k_{20}	22.48	(5)	
	Coefficient in equation (8), $\dot{\gamma}_{oo}^*$	0.705	(6), (8)	
	Exponent in equation (8), χ (J/m^3)	10.05	(8)	

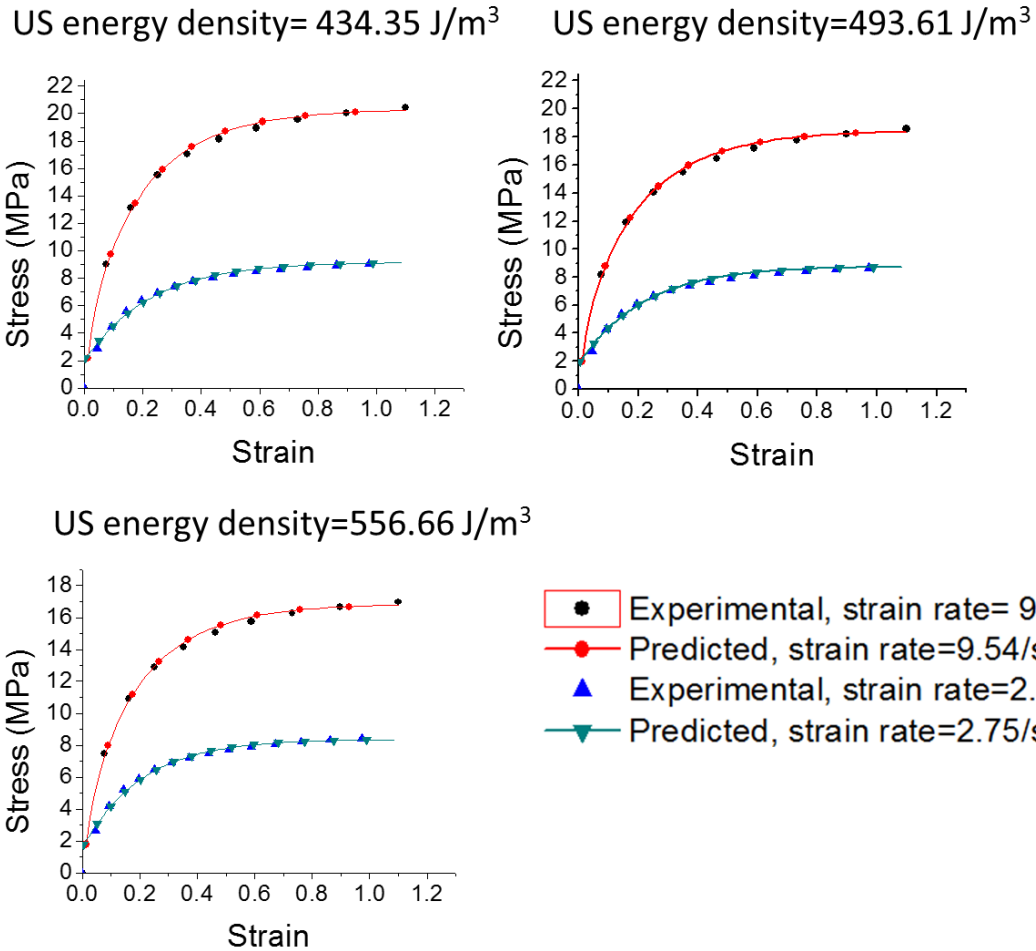


Figure 3-8. Experimental and predicted stress versus strain curves for all acoustic energy densities and strain rates.

3.5 CONCLUSIONS

One internal variable KM model described in the chapter appears to model stress evolution satisfactorily for the uniaxial compression tests conducted on pure aluminium wires. Using after-deformation microstructure analysis, an evidence of acoustic energy enabled dynamic recovery has been provided. One internal variable Kocks-Mecking model has been modified to incorporate this dynamic recovery. The chapter demonstrates an analogy between the microstructure evolution in hot deformation and that during deformation under

the influence of acoustic energy; an increase in acoustic energy density or decrease in strain rate during deformation results in an increase in subgrain size. The subgrain formation observed in the EBSD results is similar to earlier results obtained by Siu et al. and, Westmacott and Langenecker [45] [46]. The dynamic dislocation simulation performed by Siu et al. also provides an evidence for an increase in dislocation annihilation which corroborates the hypothesis presented in this chapter [45]. The trend of dislocation annihilation also in the dynamic dislocation simulations also appears to be similar to the predicted trend in this chapter. An interesting key difference between hot deformation and acoustic energy assisted deformation has been highlighted by Siu et al. According to their experiments and simulations, just the application of acoustic energy cannot enable recovery in a material unlike heat energy which can enable recovery in a material without simultaneous application of a stress field. In other words, acoustic energy enables recovery only when applied in conjunction with a stress field.

The graph for predicted dislocation density versus strain in the chapter is different from that predicted by Yao et al. [31], but appears to be phenomenologically more accurate.

The obtained results in the chapter can be extended to applications like wire bonding, ultrasonic assisted wire drawing, ultrasonic assisted forming and ultrasonic consolidation where the acoustic energy induced plasticity plays an important role.

CHAPTER 4

MICROSTRUCTURE EVOLUTION OF FCC METALS DURING ULTRASONIC ENERGY ASSISTED DEFORMATION

4.1 INTRODUCTION

Since the discovery of the ultrasonic softening phenomenon, the effect of ultrasonic energy on the flow stresses during plastic deformation has been investigated and attempts have been to model the behavior by several researchers [29] [47] [31]. The main focus of most of the investigations has been aluminum or aluminum alloys. Nevertheless, the fundamental understanding of the physics of the softening phenomenon is still incomplete, especially with regards to its effects on the microstructure evolution during deformation process. This understanding of microstructure evolution is critical since the post-deformation microstructure determines the mechanical properties of the deformed metal. Some efforts have been made to this end by researchers. In the context of ultrasonic welding or ultrasonic consolidation, the focus in the literature has been on analyzing the microstructure at the interface between the welded materials [48] [49]. In such studies conducted at the interface, it becomes difficult to decouple the impact of frictional heating and ultrasonic energy on the microstructure evolution. Zhou et al. used Electron Backscatter Diffraction Analysis (EBSD) to compare the after-deformation microstructure of aluminum and titanium after ultrasonic-assisted compression [50]. Siu et. al. used EBSD and TEM analysis to investigate the microstructure and dislocation substructure of aluminum after ultrasonic energy assisted indentation, and dislocation dynamic simulation was used to hypothesize that ultrasonic energy provides a superimposed oscillatory stress

which helps in dislocation annihilation. Similar annihilation of dislocations during ultrasonic energy assisted deformation, which led to coarsening of the subgrain network, was observed in the study in the previous chapter.

In this chapter, the effect of stacking fault energy on the microstructure evolution during ultrasonic energy assisted compression has been investigated using EBSD and TEM analysis of aluminum, copper and aluminum 6061 alloy. An analogy between the resulting microstructure post hot deformation and ultrasonic assisted deformation has been shown. A thorough analysis through a comparison between high stacking fault energy material (aluminum) and medium stacking fault energy material (copper) has been presented.

The effect of stacking fault energy on microstructure evolution during hot working of metals is well understood. For FCC materials, the motion of dislocations in the (111) closed packed slip plane happens along the $\langle 110 \rangle$ direction. Whether the motion of dislocations happens as perfect dislocations or through dissociation of dislocations into 2 partial dislocation (Shockley partial dislocations) is determined by the stacking fault energy of the material. For metals like gold, nickel and copper with low to medium stacking fault energy, the motion of dislocation by dissociation into 2 partials is favored since the energy required to generate the wide stacking fault associated with dissociation is lesser. The dissociation and formation of this stacking fault inhibits climb and cross-slip which restricts recovery and results in an increase in dislocation density. Beyond a certain limit, the local difference in dislocation density results in grain nucleation. This phenomenon of new grain nucleation and growth during deformation is called discontinuous dynamic recrystallization (DDRX). For high stacking fault energy materials like aluminum, the dissociation of dislocations is not energetically preferred. Hence the motion of dislocation happens as perfect dislocations

or with a stacking fault with a very small width. This promotes climb and cross-slip, facilitating dynamic recovery (DRV). The resulting microstructure in the high stacking fault energy materials contains subgrains with grain interiors having much lower dislocation densities [32] [51]. However, aluminum and aluminum alloys have been shown to exhibit recrystallization behavior during hot deformation. This unique recrystallization behavior is caused by formation of serrated grain boundaries due to subgrains and subsequent pinching-off of these serrated grain boundaries at a high enough strain which results in formation of new grains. This type of recrystallization is called geometric dynamic recrystallization (gDRX) [32] [51] [52].

A similar fundamental understanding and analysis for post-deformation microstructure of materials deformed under the influence of ultrasonic energy is crucial for the wide spread-application and use of ultrasonic energy in manufacturing processes. The work presented in this chapter provides a detailed insight into the effect of ultrasonic energy on microstructure evolution of FCC metals with different stacking fault energies. The insight reported here will also advance current understanding of parameter-microstructure-mechanical property correlations for manufacturing techniques such as wire bonding, ultrasonic consolidation, and ultrasound-assisted incremental forming.

4.2 EXPERIMENTAL METHODS

4.2.1 APPARATUS

The same apparatus as described in the earlier chapter was used for all the experiments. For all sets of experiments, the resonant frequency of the system is designed to be 40 kHz. For all the experiments performed, a constant strain rate of 6s^{-1} was used. The amount of ultrasonic energy density applied to the metal filament during compression was controlled

by varying the amplitude of vibration of the ultrasonic energy coupling tool. The ultrasonic energy density was calculated using the formula, $E = a^2\omega^2\rho$, where a is the vibration amplitude measured at the tip of the ultrasonic energy coupling using a vibrometer, ω is the vibration amplitude in rad/s and ρ in kg/m^3 is the density of the filament being deformed.

4.2.2 SAMPLE PREPARATION FOR MICROSTRUCTURAL ANALYSIS

Copper and Al6061 filaments were deformed under the application of two different ultrasonic energy densities (500 J/m^3 and 710 J/m^3 for copper and 150 J/m^3 and 215 J/m^3 for Al6061). A cross section of the deformed filaments was cut, and standard polishing sequence was followed to prepare the samples for EBSD analysis. The samples were initially embedded in a two-part epoxy resin for convenience during polishing. Beginning with a 320 grit SiC abrasive paper, the samples were mechanically polished by abrasive papers of increasing grit up to 1200 grit. This was followed by polishing with $3 \mu\text{m}$ polycrystalline diamond slurry, $0.5 \mu\text{m}$ polycrystalline diamond slurry and $0.05 \mu\text{m}$ colloidal silica slurry. The final polishing step was to polish the samples in a vibratory polisher for 4-5 hours using $0.05 \mu\text{m}$ colloidal silica slurry. Samples were cleaned in an ultrasonic bath between each polishing step. These samples were then analyzed on a FEI Nova600 FEG-SEM equipped with an EDAX EBSD detector. The EBSD maps generated were imported in OIM analysis software for data presentation and analysis.

4.2.3 SAMPLE PREPARATION FOR TEM ANALYSIS

To prepare samples for TEM analysis, a cross section of the sample along the length of the wire was cut. Same sample preparation method as described above was used to polish the samples. A FEI Helios Nanolab 660 dual beam Focused Ion Beam (FIB) was used to lift-

out an electron transparent lamella of the sample. To do this, a protective platinum layer was deposited on the region of interest. Two trenches were milled on either side of the region of interest. The lamella (or region of interest) was then welded to a needle and separated from the bulk material. The lamella was transferred onto a copper half grid and further thinning was performed at low beam current. The lamellas so prepared were analyzed in a 200 kV FEI Tecnai F20 TEM/STEM equipped with an EDAX EDS detector.

4.3 RESULTS AND DISCUSSION

4.3.1 MICROSTRUCTURAL ANALYSIS OF COPPER

Figure 4-1 shows inverse pole figure (IPF) maps of undeformed copper wire, wire deformed without ultrasonic energy, and wire deformed with two different ultrasonic energy densities (500 J/m^3 and 710 J/m^3) and at a strain of 0.51 and 0.75. Misorientations in the maps are with reference to the direction of compression, represented by the A1 axis. The average grain size of the undeformed wire is $3.68 \text{ }\mu\text{m}$ with isotropic grains. The undeformed wire consists of annealing twins marked by red lines in Figure 4-1a. After deformation, grains appear to be flattened and the grain size decreases to $0.89 \text{ }\mu\text{m}$ for deformation without ultrasonic energy assistance. For deformation in the presence of ultrasonic energy, the average grain size is higher than that for deformation without ultrasonic energy. Also, the average grain size increases, albeit only slightly, with an increase in ultrasonic energy density applied during deformation. Figure 4-1c and Figure 4-1d show formation of small grains in the vicinity of grain boundaries of larger grains.

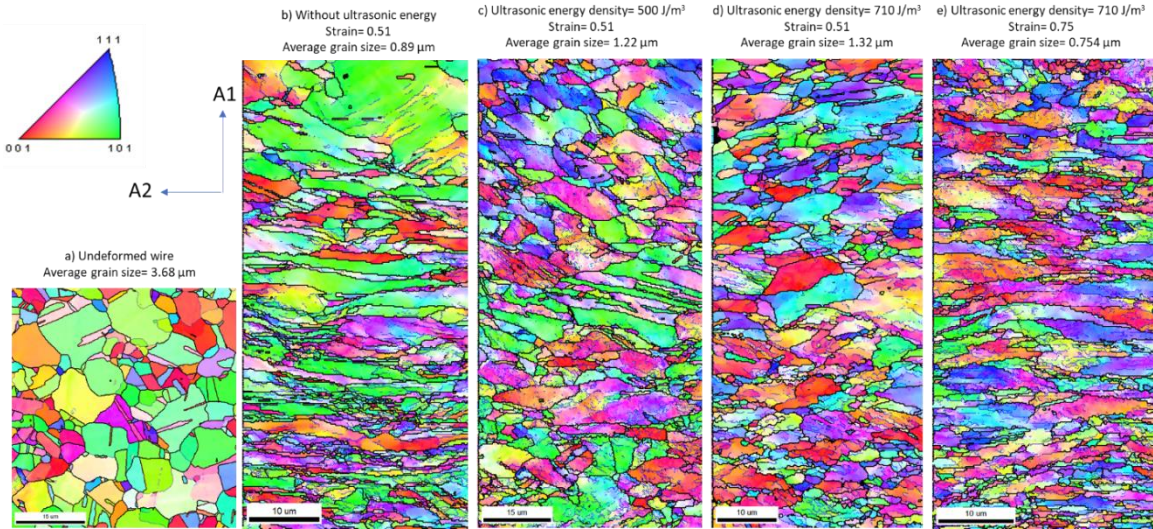


Figure 4-1. EBSD map of a) Undeformed copper wire, b) copper wire deformed without any ultrasonic energy assistance, c) copper wire deformed with 500 J/m³ ultrasonic energy density, copper wire deformed with 710 J/m³ ultrasonic energy density and d) copper wire deformed with 710 J/m³ ultrasonic energy density to a higher compressive strain of 0.75. High angle grain boundaries are highlighted by thick black lines while low angle grain boundaries (or subgrain boundaries) are highlighted by thin blue lines. A1 represents the direction of compression.

Figure 4-2 shows the grain orientation spread map for the EBSD maps shown in Figure 4-1. Grain orientation spread of each grain is calculated using the OIM software by first, calculating the average orientation of the grain. Then, misorientation of each pixel within the grain with respect to the average orientation of the entire grain is calculated. The average of all such misorientations within the grain determines the grain orientation spread of an individual grain. The formula used is given by $GOS(i) = \frac{1}{J(i)} \sum_j \omega_{ij}$, where $J(i)$ is the number of pixels in grain i , ω_{ij} is the misorientation angle between the orientation of pixel j and the average orientation of the grain i [53]. Typically, newly formed

recrystallized grains have low deformation structure within them. Hence a low GOS value of 0-1.5 indicates a recrystallized grain, while values higher than 1.5 indicate deformed grains. As is evident from Figure 4-2, there is an increase in the fraction of recrystallized grains (represented in blue color) from 0.041 for deformation in absence of ultrasonic energy to ~0.068 for deformation in the presence of ultrasonic energy. With an increase in strain from 0.51 to 0.75, the fraction of recrystallized grains increases further to 0.125. The size of the recrystallized grains increases for deformation in presence of ultrasonic energy as well as with increase in acoustic energy during deformation.

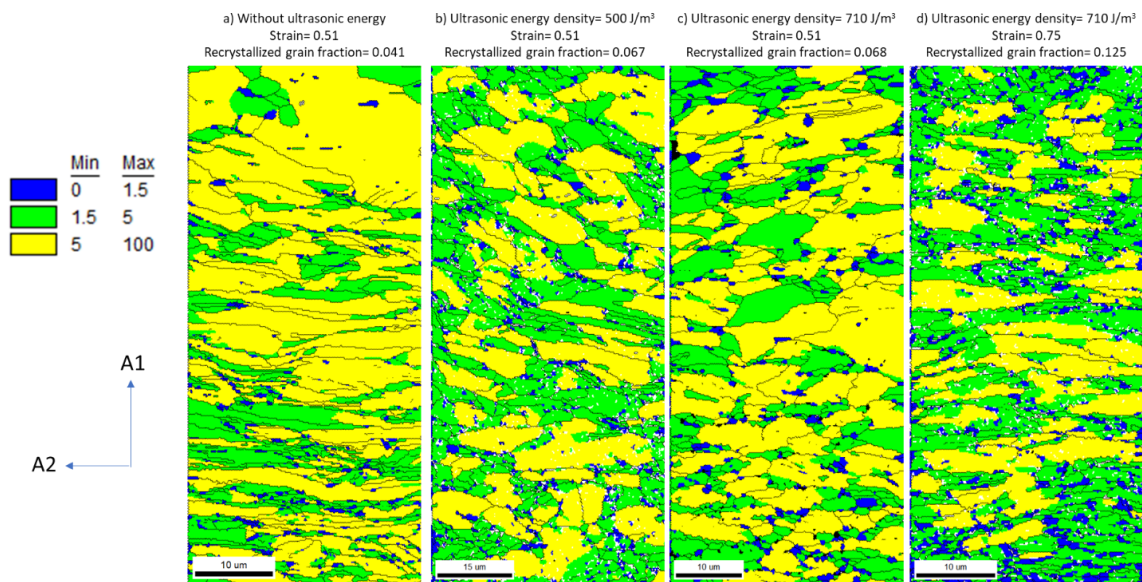


Figure 4-2. Grain orientation spread (GOS) map of a) copper wire deformed without any ultrasonic energy assistance, b) copper wire deformed with 500 J/m³ ultrasonic energy density, c) copper wire deformed with 710 J/m³ ultrasonic energy density and d) copper wire deformed with 710 J/m³ ultrasonic energy density to a higher compressive strain of 0.75. The blue grains have average GOS between 0-1.5, green ones have average GOS between 1.5-5 and yellow ones have average GOS between 5-100.

TEM bright field images for copper sample deformed under the presence of ultrasonic energy (US energy density= 500 J/m³) are shown in Figure 4-3. The flattened substructure with a very high dislocation density in the interior is clearly evident from the Figure 4-3a. Figure 4-3b shows recrystallized grain in the substructure which has very different orientation as compared to the rest of the substructure evident by the contrast. The dislocation density in this grain is also relatively lower than rest of the substructure. Figure 4-3c shows formation of low angle subgrain boundaries in the vicinity of the grain boundary of the primary grain.

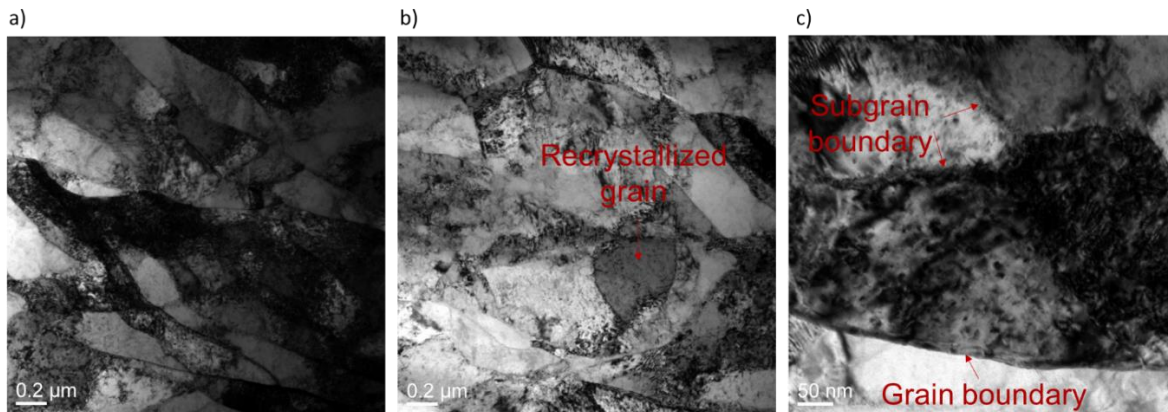


Figure 4-3. TEM bright field images of copper sample after deformation under simultaneous application of ultrasonic energy (US energy density= 500 J/m³). a) Flattened grain structure after deformation, b) Recrystallized grain marked by red arrow and c) Subgrain boundaries formed in the vicinity of a primary grain boundary.

In warm and hot deformation of medium stacking fault energy materials like copper, as explained in the Introduction section, the lack of dynamic recovery in the material leads to local increases in the dislocation density. Of particular interest is the region near the grain boundaries where the relatively large local misorientations result in formation of potential

grain nucleation sites and eventual dynamic recrystallization of grains. A similar behavior can be observed in ultrasonic energy assisted deformation. With further deformation accompanied by dislocation entanglement in regions similar to the ones shown in Figure 4-3c, the local misorientation of these regions near the grain boundaries increases, leading to grain nucleation (grains depicted by blue color in Figure 4-2b, Figure 4-2c and Figure 4-2d).

For hot and warm deformation, it is well documented that the increase in deformation temperature or reduction in strain rate results in an increase in grain size and recrystallized grain volume fraction [51] [54] [55]. The grain size analysis shown in Figure 4-1 indicates that when thermal energy is replaced with ultrasonic energy, analogous results in microstructure evolution can be observed. The increased fraction of recrystallized grains for deformation under the presence of ultrasonic energy can be attributed to the assistance of ultrasonic energy in formation of subgrain boundaries. This subgrain formation, particularly near the grain boundaries, results in the formation of regions with local misorientations and potential grain nucleation sites. An evidence of assistance to subgrain boundary (or low angle boundary) formation due to simultaneous application of ultrasonic energy can also be seen in b, where the area fraction of low angle boundaries (first 2 columns of the histogram) for copper samples deformed with ultrasonic energy (area fraction ≈ 0.4) is significantly higher than the area fraction for copper samples deformed without ultrasonic energy (area fraction ≈ 0.19). Similar assistance to subgrain formation was observed during ultrasonic energy assisted indentation experiments by Siu et. al [45].

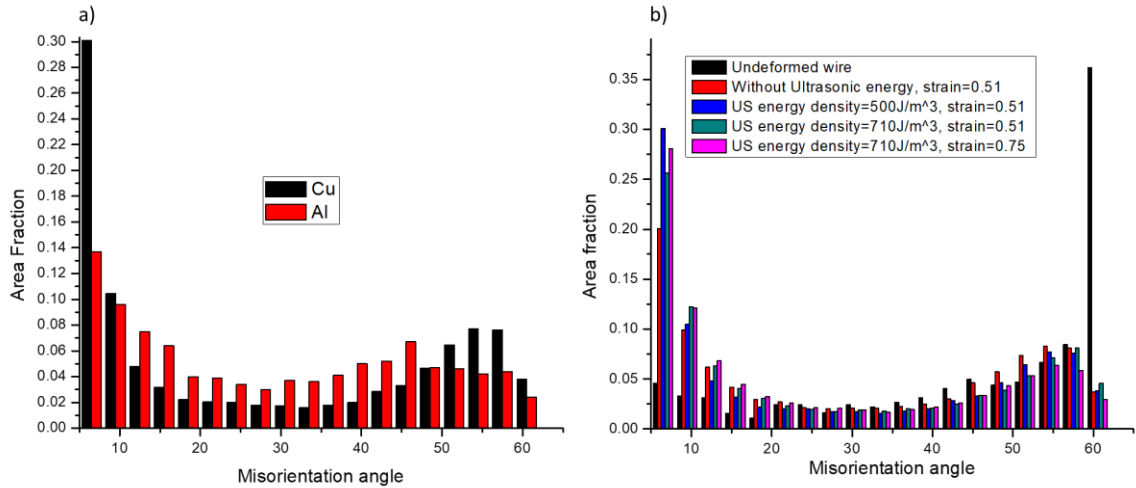


Figure 4-4. Misorientation angle versus area fraction histogram for- a) Copper and aluminum deformed under the presence of same ultrasonic energy density level and b) undeformed copper wire, copper deformed without ultrasonic energy, copper deformed in the presence of ultrasonic energy density of 500 J/m³, 710 J/m³ and copper deformed in the presence of ultrasonic energy density of 710J/m³ to a higher strain.

The complete absence of such recrystallization in aluminum after ultrasonic energy assisted deformation, as seen in Chapter 2, is because aluminum has high stacking fault energy. This promotes dynamic recovery during deformation of aluminum assisted by ultrasonic energy. Hence, although there is formation of low angle or subgrain boundaries (as seen in Figure 3-5), the low dislocation density prevents local misorientations from increasing, thereby suppressing DDRX. The very high fraction of low angle boundaries in copper as compared to aluminum, as evident from Figure 4-4a, also indicates higher local misorientations within the primary grains, which contribute to increased DDRX. Even though aluminum and copper have the same FCC crystal structure, it is the difference in

their stacking fault energies that results in a starkly different microstructure after deformation under similar conditions of ultrasonic energy density and strain rate.

Figure 4-5 shows the inverse pole figure maps for undeformed Al6061 wire and wires deformed to a strain of 0.75 under the presence of ultrasonic energy of 150 J/m^3 and 215 J/m^3 . Just as in the earlier case, misorientations in the maps are with reference to the direction of compression, represented by the A1 axis. The microstructure of the undeformed wire shows annealed grain structure with an average grain size of $6.05 \mu\text{m}$. The map shows negligible amount of subgrain boundaries. In contrast, the EBSD map of wires deformed under the presence of ultrasonic energy show substantial subgrain formation. The after-deformation grain size decreases and very fine grains appear at the grain boundaries of larger grains. For deformation using ultrasonic energy density of 150 J/m^3 , the average grain size is $0.33 \mu\text{m}$ and it increases to $0.52 \mu\text{m}$ for deformation using ultrasonic energy density of 215 J/m^3 .

The corresponding grain orientation spread maps of the EBSD maps in Figure 4-5 are shown in Figure 4-6. A very high fraction of recrystallized grains (~ 0.36), depicted by blue color, can be seen in the GOS maps. Although it might appear from this particular map that the fraction of recrystallized grains is higher for sample deformed with ultrasonic energy density of 150 J/m^3 , the overall average of several such maps showed that there was no significant change in the fraction of recrystallized grains with the change in ultrasonic energy density.

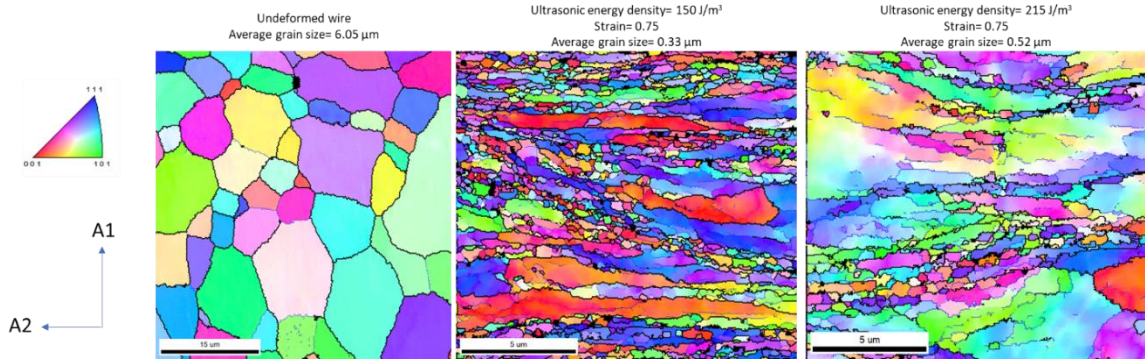


Figure 4-5. Inverse pole figure maps of a) Undeformed Al6061 wires, b) Al6061 wire deformed under the presence of ultrasonic energy density of 150 J/m³ and c) Al6061 wire deformed under the presence of ultrasonic energy density of 215 J/m³, b) and c) both compressed to a strain of 0.75. High angle grain boundaries are highlighted by thick black lines while low angle grain boundaries (or subgrain boundaries) are highlighted by thin blue lines. A1 represents the direction of compression.

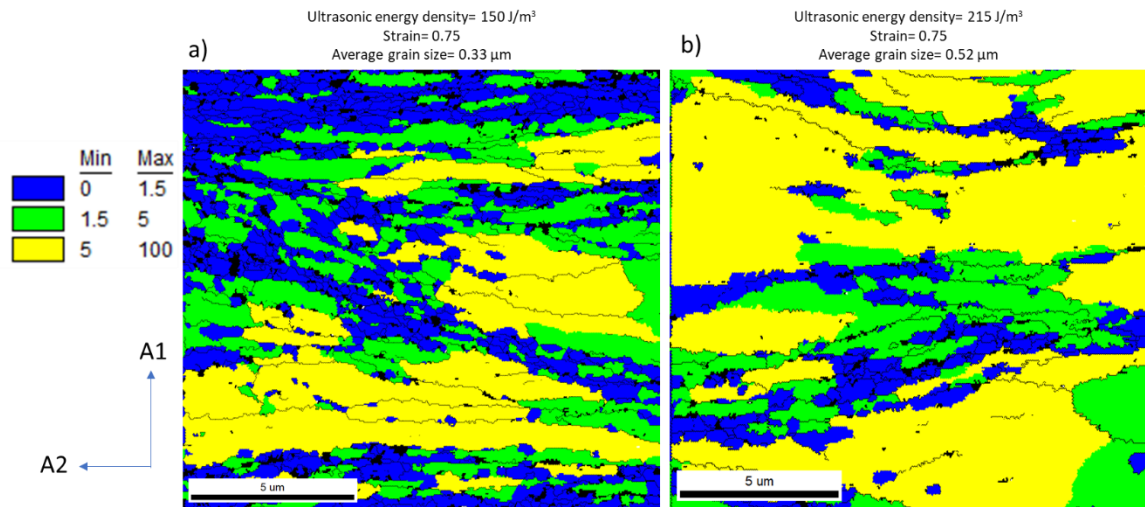


Figure 4-6. Grain orientation spread (GOS) map of- a) Al6061 wire deformed with 150 J/m³ ultrasonic energy density and b) Al6061 wire deformed with 215 J/m³. The blue grains have average GOS between 0-1.5, green ones have average GOS between 1.5-5 and yellow ones have average GOS between 5-100.

The STEM image in Figure 4-7a shows a classical recrystallization microstructure with a larger grain surrounded by smaller recrystallized grains. Al6061 alloy is a precipitation hardened Al-Mg-Si alloy. The Mg_2Si precipitates in the alloy provide hindrance to dislocation motion [56]. These precipitates are shown in Figure 4-7b, marked by red arrows. An EDS map of the sample shown in Figure 4-8, illustrates the elemental distribution in the precipitates and the matrix. It can be seen that Si, Cr and Fe are concentrated in the precipitates while Mg and Cu are distributed uniformly. Some precipitates are richer in Cr and Fe as seen from the two tables which show the quantitative EDS analysis in the respective precipitates shown in the electron image (precipitate 2 is richer than precipitate 1). In Figure 4-7c, a subgrain boundary formed by entangled dislocations (marked by red arrow) can be seen along with other dislocations within the subgrain. The overall dislocation density is much lower than that observed for copper samples.

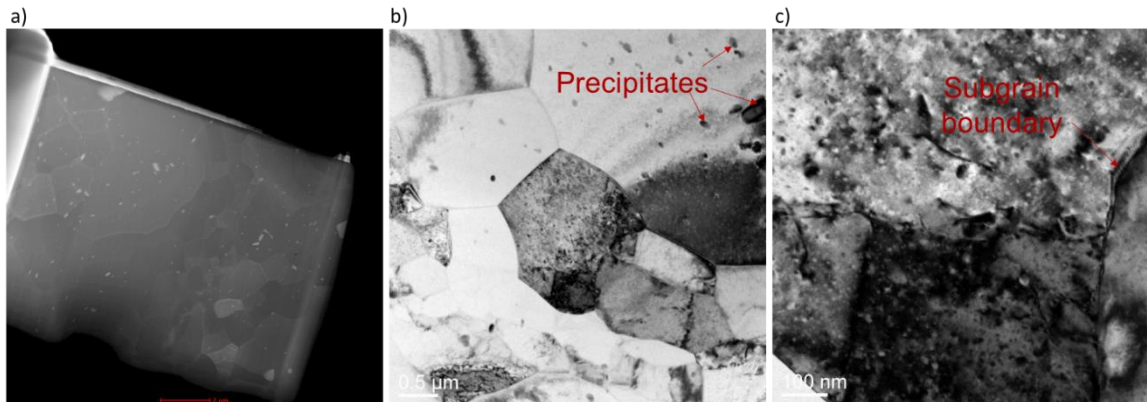


Figure 4-7. a) STEM image of Al6061 wire deformed with 210 J/m³ ultrasonic energy density, b) bright field TEM image of the same sample showing precipitates and, c) bright field TEM image showing subgrain boundary.

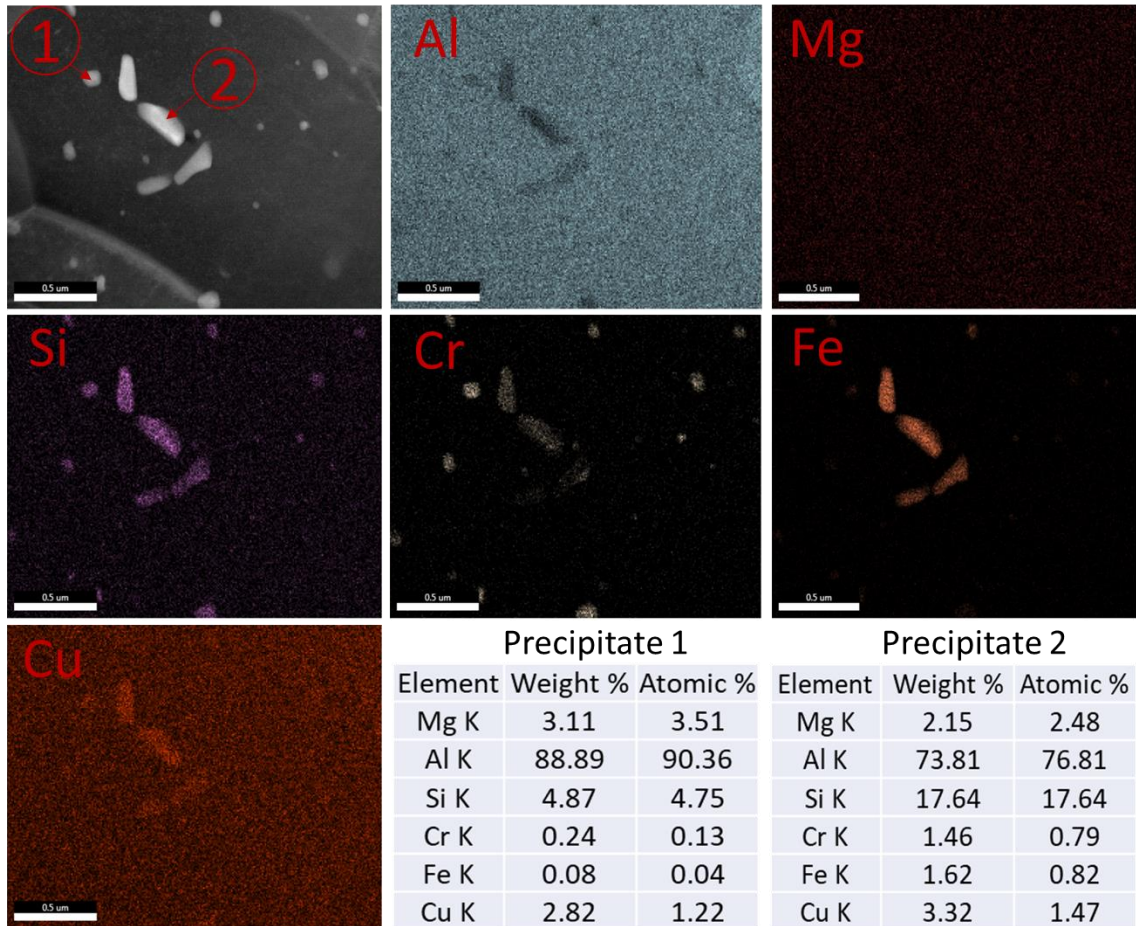


Figure 4-8. EDS map of the Al6061 sample deformed with 210 J/m³ ultrasonic energy density. Table show the quantitative EDS point analysis for the 2 precipitates shown in the electron image.

The grain refinement observed in the post-deformation microstructure of samples deformed under simultaneous application of ultrasonic energy (Figure 4-5) can be attributed to the recrystallization, as observed in Figure 4-6. Although aluminum alloys have a high stacking fault energy, these alloys have shown to undergo recrystallization during hot deformation. The recrystallization is caused by formation of serrated grain

boundaries which get pinched during deformation. This pinching results in formation of small grains of the order of subgrains at the boundaries of larger grains. This phenomenon called geometric dynamic recrystallization (gDRX) has been observed for aluminum alloys [52] [57] [58].

As argued before, recrystallization was not observed in Aluminum under similar conditions of ultrasonic energy and strain rate (Chapter 2). There are two possible explanations for observation of gDRX in Al6061 and not in pure aluminum. Al6061 alloys contain precipitates which obstruct dislocation motion. This thereby causes dislocation pile-up and generation of new dislocations at the precipitates, as shown in Figure 4-7b and Figure 4-7c. Interaction of local dislocations with pile-ups results in subsequent formation of subgrains, which in fact are the cause for formation of serrated grain boundaries [58]. The second factor is that the initial average grain size of the undeformed pure aluminum wire was $\sim 10 \mu\text{m}$ while the average size of the undeformed Al6061 wire was $\sim 6 \mu\text{m}$. It has been observed during hot deformation process that the reduction in initial grain size facilitate the initiation of gDRX at a lower value of strain [52]. During compression, the width (i.e. dimension along the compression direction) of grains with smaller initial size approaches the subgrain size at a lower strain value. Hence, the pinching-off of subgrains and subsequent gDRX happens at a lower strain value than that for grains with larger initial size. Hence, the smaller grain size of Al6061 wire definitely contributed to the observation of gDRX in Al6061. But whether it was the only factor or whether the precipitates in Al6061 also played a role in this process requires further investigation.

The assistance to subgrain formation due to simultaneous application of ultrasonic energy is evident from the misorientation angle versus area fraction graph shown in Figure 4-9a.

The fraction of subgrain boundaries or low angle boundaries (first 2 columns in the histogram) increases significantly with an increase in ultrasonic energy density. The average grain size and the size of the grains which have gone through gDRX depends on the subgrain size [52]. It was observed in [59] that for pure aluminum, the subgrain size increases with an increase in ultrasonic energy density due to coarsening of subgrain network caused by assistance of ultrasonic energy to dislocation annihilation. For Al6061, the increase in average grain size and the size of recrystallized grains (Figure 4-5) with an increase in ultrasonic energy density can be attributed to this increase in subgrain size. The lesser fraction of subgrain boundaries for Al6061 as compared to pure aluminum, evident from Figure 4-9b, is due to gDRX of subgrains which transforms subgrain boundaries into high angle boundaries.

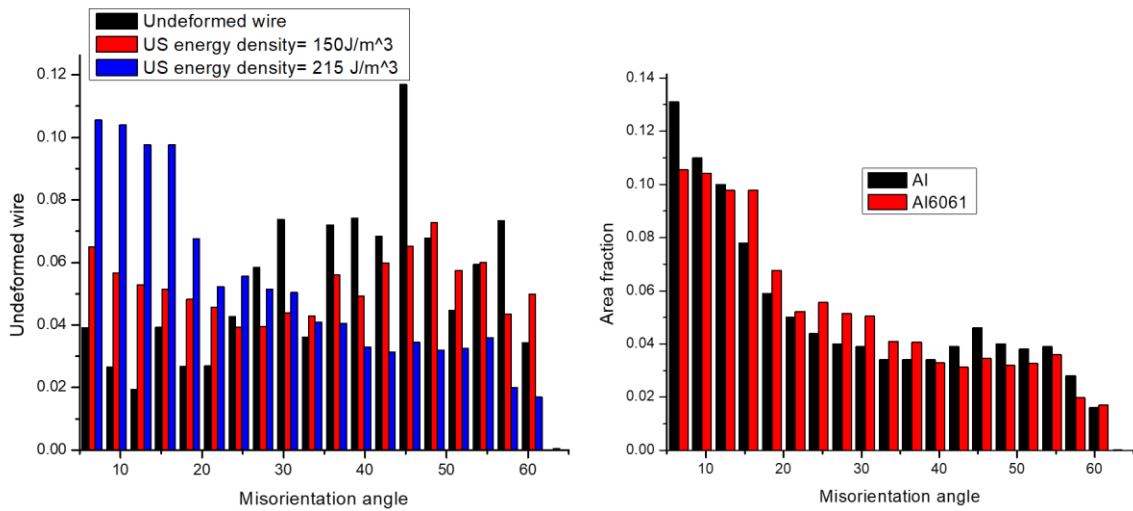


Figure 4-9. Misorientation angle versus area fraction histogram for- a) undeformed Al6061 wire, Al6061 wire deformed under ultrasonic energy density of 150 J/m³ and 215 J/m³, b) Aluminum and Al6061 deformed under similar conditions of ultrasonic energy density.

4.4 CONCLUSION

In this chapter, a detailed analysis of the effect of stacking fault energy on the microstructure of FCC metals during ultrasonic energy assisted deformation was conducted. It was observed that ultrasonic energy assists in subgrain formation, which is in line with earlier observations made in the literature [45]. A comparison of microstructure of medium stacking fault energy metal (copper) and high stacking fault energy metal (aluminum from previous studies) was made using EBSD and TEM analysis. For copper, which is a medium stacking fault energy metal, lack of dynamic recovery resulted in high dislocation density. Evidence of discontinuous dynamic recrystallization (DDR_X) was observed analogous to that in hot deformation. For Al6061, geometric dynamic recrystallization (gDR_X) was also observed after ultrasonic energy assisted deformation.

The insights reported here improves upon the current understanding of the effect of ultrasonic energy irradiation during deformation on the microstructure of FCC metals. It advances the understanding of correlation between the post-processing microstructure and deformation conditions for processes such as ultrasonic consolidation, ultrasound-assisted incremental forming, wire bonding and other ultrasonic energy assisted forming processes. A deeper understanding of ultrasonic energy-metal interaction derived from this work will help to increase the adoption of ultrasonic energy in the manufacturing industry.

CHAPTER 5

IN-PROCESS MICROSTRUCTURE TUNING IN SOLID-STATE AMBIENT CONDITION METAL DIRECT MANUFACTURING

5.1 INTRODUCTION

In current powder-based metal additive manufacturing processes, temperature gradient in the components along the build direction results in the formation of elongated grains in the build direction. This epitaxial grain growth results in part property anisotropy [60] [61]. Typically, post-processing heat-treatment is performed on the components to alter the microstructure. There have been some efforts to achieve in-process microstructure control during PBF processes by monitoring the melt pool size and then adaptively controlling process parameters like laser power and scan speed [62]. But actual in-process monitoring and microstructure control is still a distant goal for PBF processes.

One characteristic of AMD is that it allows for the possibility of voxel-by-voxel in-process microstructure control. As mentioned before, acoustic softening enables the shaping of the filament voxel, and acoustic energy assisted mass transport results in formation of metallurgical bonds between the filament and the lower layer. This process is repeated to additively fabricate a 3-dimensional object voxel-by-voxel in a direct write fashion. By controlling the acoustic energy density input to the material and the strain rate during deformation, the microstructure of each voxel can be controlled in-process.

As described in chapter 3, irradiation of acoustic energy during material deformation causes an acoustic energy enabled dynamic recovery in the material due to assistance

provided to dislocation annihilation by acoustic energy. Deformation under the influence of higher acoustic energy density results in more dislocation annihilation and hence, a proportional increase in softening is observed for deformations under the influence of higher acoustic energy densities. The same is true for deformation at slower strain rates. The acoustic energy enabled dynamic recovery also enables formation of subgrains. The size of these subgrains increases with an increase in the acoustic energy density applied during deformation or with reduction in strain rate during deformation as shown in Chapter 3. Hence, by changing the ultrasonic energy density and/or strain rate during voxel deposition, the subgrain size in each voxel can be controlled.

In this chapter, the microstructure evolution after deposition of each successive layer has been described to understand the microstructure evolution process during AMD in its entirety. Aluminum samples with three layers were fabricated using AMD. Electron Backscatter Diffraction (EBSD) analysis on each layer of the sample was conducted. Microhardness measurements were also performed on each layer of the sample to analyze the mechanical property evolution during the material deposition process. A comparison of the microstructure between SLM process and AMD process has been presented. The effect of phase change on the microstructure in case of SLM process and the subsequent differences with solid-state AMD process are highlighted using an example of a SLM printed Nickel based superalloy Inconel 718. Although the materials being compared are different, the comparison intends to provide a process-microstructure correlation.

5.2 EXPERIMENTAL METHODS

5.2.1 SAMPLE PREPARATION FOR EBSD

Experimental setup described in Chapter 2 was used to build aluminum samples. To study the microstructure, samples with 1-, 2- and 3-layers were built. The samples were sectioned and polished with similar steps described in Chapter 3 and Chapter 4. After the samples were polished, Electron Backscatter Diffraction (EBSD) analysis was performed on each layer of the samples.

5.2.2 MICROHARDNESS MEASUREMENT

Vickers microhardness tests were performed on each layer of the samples polished according to the procedure described in the earlier section. 10 micro-indentations were made at the center of each layer using a force of 98.07 mN. Figure 5-1 shows an example of an indentation created during the tests. The mean of the length of two diagonals of the indents was calculated to obtain the hardness values using the formula, $HV = \frac{2F \sin\left(\frac{136}{2}\right)}{d^2}$, where F is the force in kgf and d is the mean of the lengths of two diagonals of the indents.

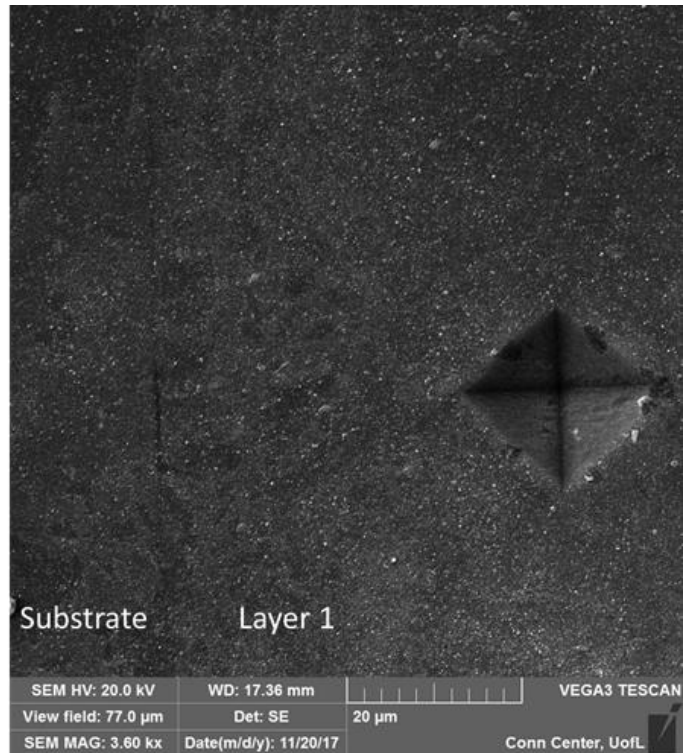


Figure 5-1. Figure showing an example of indentation created during the Vickers microhardness test.

5.3 RESULTS AND DISCUSSION

5.3.1 MICROSTRUCTURE EVOLUTION DURING AMD PROCESS

In AMD, large amounts of plastic deformation in the filament during voxel formation results in a flow of material in the lateral directions. This flow of material helps to achieve inter-filament diffusion. In some cases, due to the inaccuracy of the filament positioning mechanism in the current experimental setup, a void is formed in the region of the inter-filament interface. Efforts are being made to improve the current experimental setup in order to eliminate this inconsistency.

Shown in Figure 5-2 are results of a three-layer sample fabricated using AMD. EBSD scans at each layer show similar microstructure and grain size in all the layers. Average grain

size of 2.2 micron was observed. Misorientation histograms for each layer shown in Figure 5-3 indicate a high number of low angle grain boundaries as observed in Chapter 3. But, no significant change in the misorientation is observed across the layers. Similar microstructure across all layers indicates that there is negligible effect of addition of more material on the microstructure of the lower layers, unlike PBF processes in which addition of more material results in epitaxial grain growth along the build direction, which results in anisotropic part properties [60] [63].

During the voxel deformation and bonding under the influence of acoustic energy in AMD, the acoustic energy enabled dynamic recovery enables to control the microstructure of each voxel and hence the whole component, by controlling the acoustic energy density and the strain rate. As mentioned before in the Introduction section, increase in acoustic energy density or decrease in the strain rate results in an increase in the subgrain size after deformation. The details of the effect of acoustic energy density and strain rate on the microstructure have been described in detail in Chapter 3. Hence, by manipulating the acoustic energy density and/or strain rate, the microstructure, more specifically the subgrain size, of each voxel and hence the whole component can be controlled. Since the deformation and metallurgical bonding are athermal phenomenon, the complications due to repeated thermal cycling in the components and its resulting effects on microstructure are eliminated.

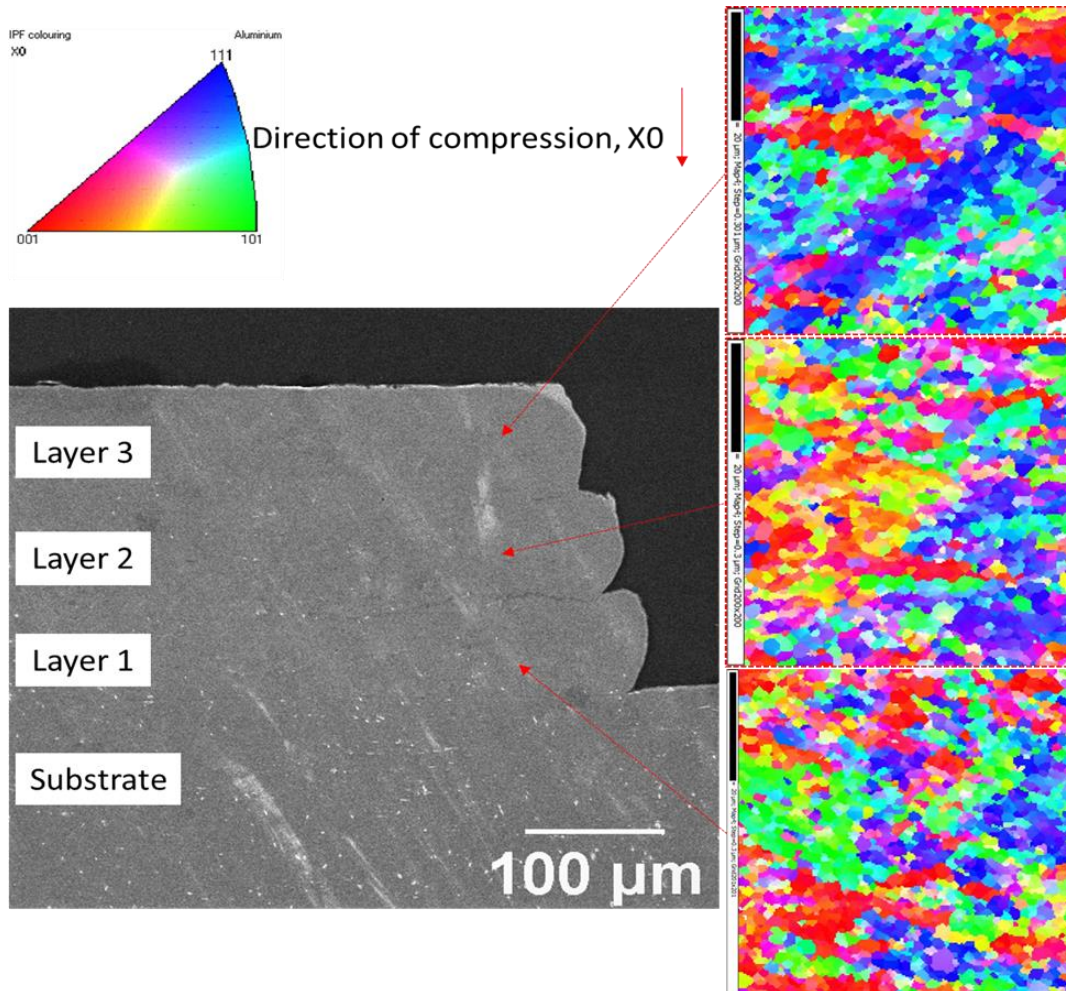


Figure 5-2. 3-layer sample fabricated using AMD and IPF images for each of the three layers.

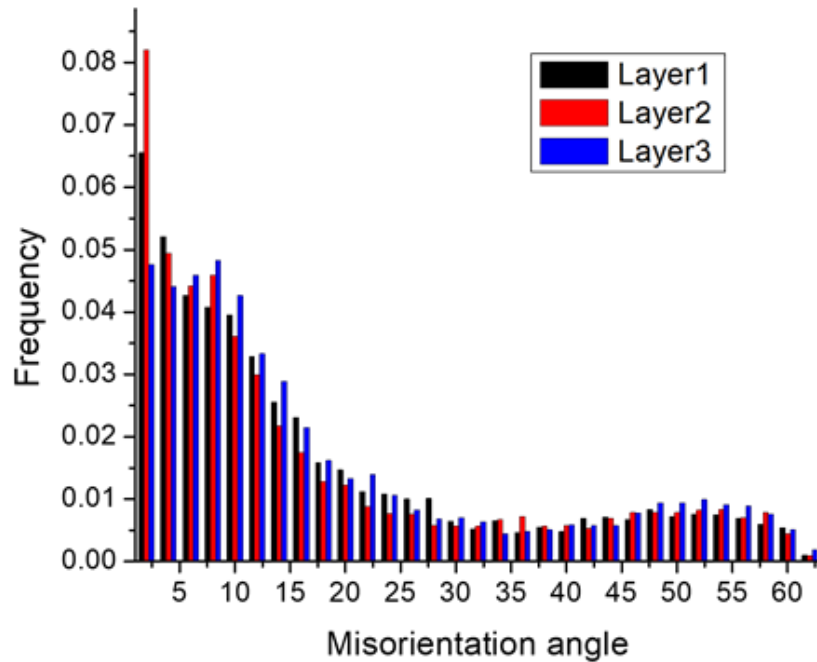


Figure 5-3. Misorientation data for 3 layers of a sample fabricated using AMD.

During voxel deposition, material in contact with the lower layer (or substrate) experiences severe plastic deformation. Due to this, small nanometer scale grains are formed at the interface. These grains are beyond the indexing resolution of EBSD. Hence the region appears as a black line in the EBSD map as shown in Figure 5-4. But beyond the small nanometer scale region, the microstructure of the substrate remains unaffected.

Figure 5-5 shows the Vickers hardness variation in the 3 layers of the sample. It is evident from the graph that there is no significant variation in the hardness in the 3 layers of the sample indicating similar mechanical properties across the whole sample.

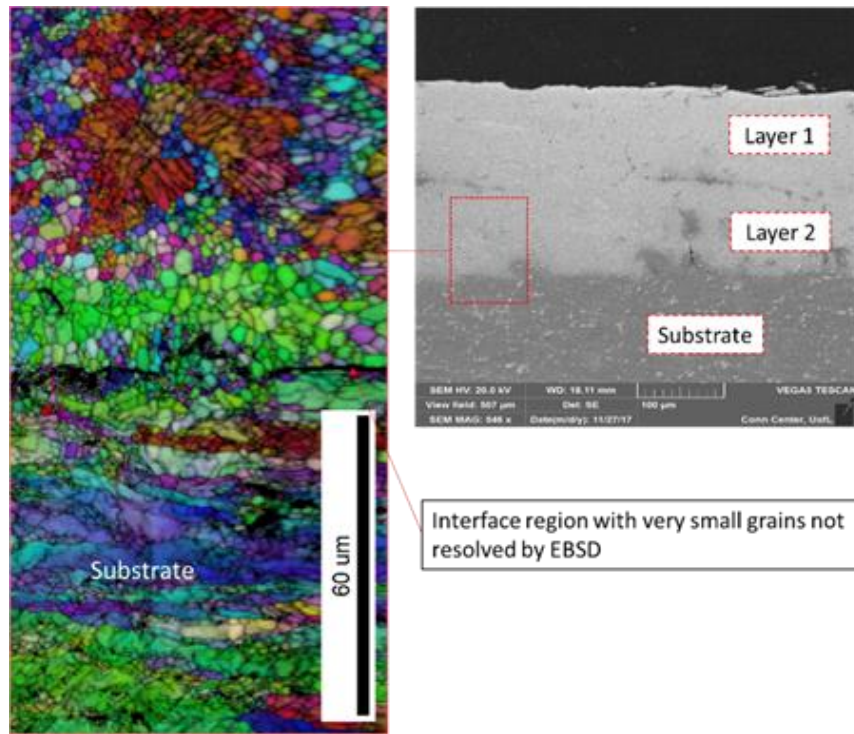


Figure 5-4. EBSD micrograph taken at the interface between first layer and the substrate.

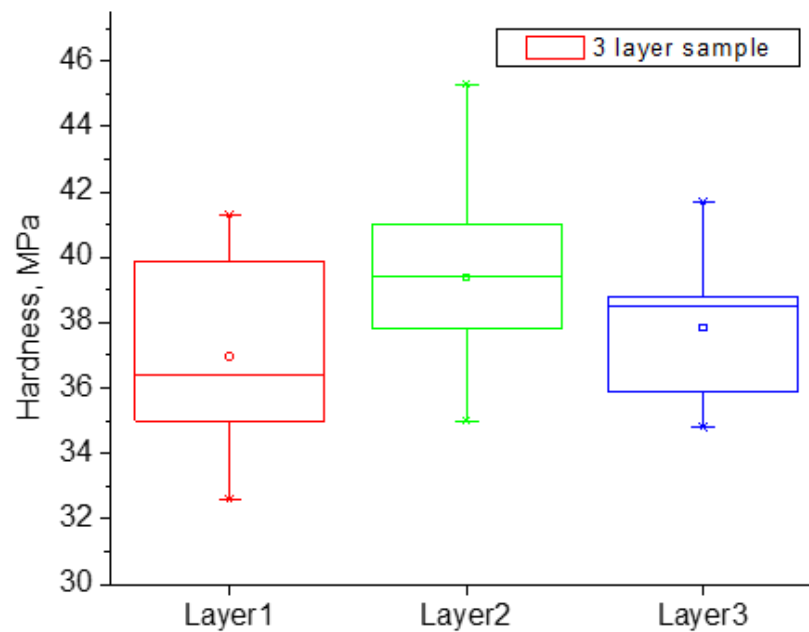


Figure 5-5. Figure shows the hardness variation across 3 layers in a sample fabricated using AMD.

5.3.2 MICROSTRUCTURE USING SLM PROCESS AND ITS COMPARISON WITH AMD PROCESS

Selective Laser Melting (SLM) is a process in which a layer of metal powder is spread on a build plate. A high-power laser scans a part of this layer melting and subsequently fusing the separate powder particles to form a solid layer. This process is repeated to form a 3-dimensional object. Typically, the melt pool depth extends across 2-3 previous layers depending on the process parameters being used. The rapid heating, followed by rapid cooling and solidification has very peculiar effects on the microstructure of the part being built. In case of Ni-based superalloy IN718, the direct result of this is that all the solute elements present beyond the solubility limit get ejected during solidification to form dendritic structures as shown in Figure 5-6. Similar structures have been observed in aluminum alloys like AlSi10Mg. Figure 5-7 shows the dendritic structures observed in AlSi10Mg samples printed using SLM process [64]. Another consequence of the phase change is that additional latent heat for phase change has to be supplied to the material.

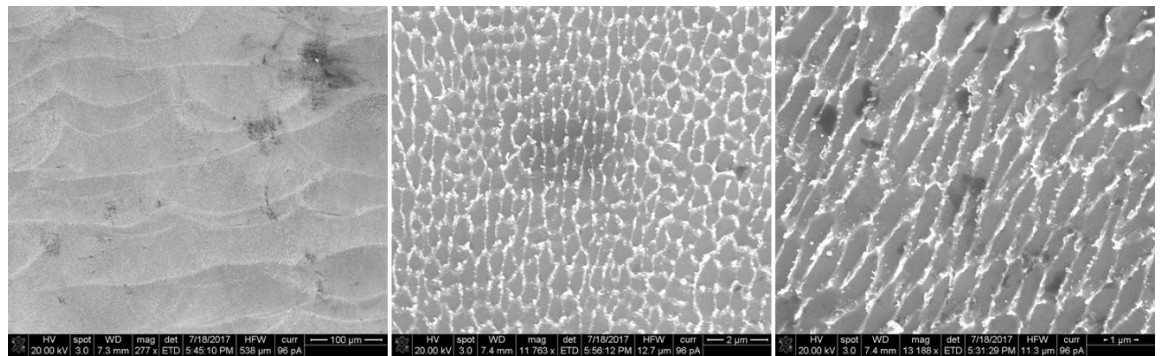


Figure 5-6. SEM images of a IN718 sample printed using SLM process showing the formation of dendritic phases.

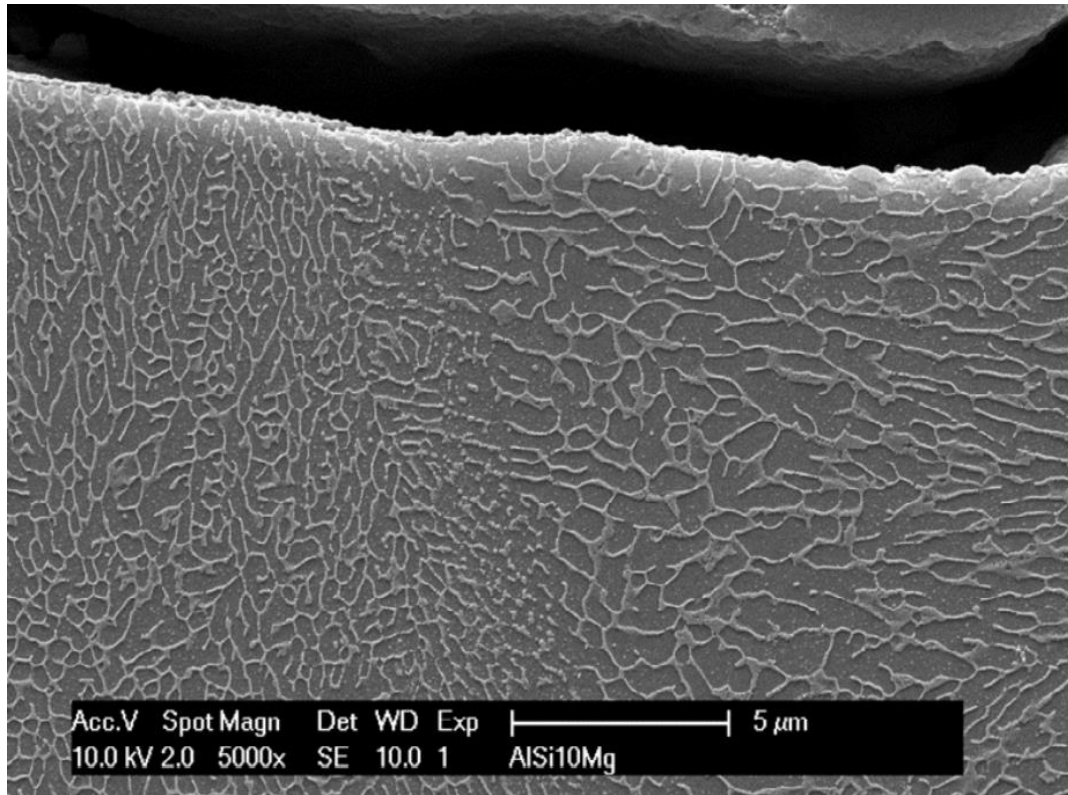


Figure 5-7. Figure shows the dendritic structure formed in AlSi10Mg sample printed using SLM process [64].

As opposed to this, in a solid-state process like AMD, the manipulation of material does not require a phase change. Also, the acoustic energy remains concentrated in the voxel being deformed as opposed to heat energy that gets dissipated. This enables the use of much lower energy densities when using the AMD process. For example, the energy density used to print components shown in Figure 2-3 is $\sim 500 \text{ J/m}^3$, whereas, for printing pure Aluminum, energy densities of the order of 10^{11} J/m^3 (or 100 J/mm^3) have to be used, especially because of the high thermal conductivity of aluminum and its alloys.

The other characteristic feature of parts made using SLM process arising from the thermal history is the microstructure. When the laser scans one track, the edges of the melt pool

have a higher heat dissipation rate and hence cool faster. This results in grain nucleation from the edge of the melt pool which grow inwards as seen in Figure 5-8a. In a bulk sample, the repeated heating of the top layer of the sample results in a thermal gradient in the build direction. This causes epitaxial growth of the grains as seen in Figure 5-8b. The consequence is that the grains are longer in the build direction resulting in anisotropic mechanical properties.

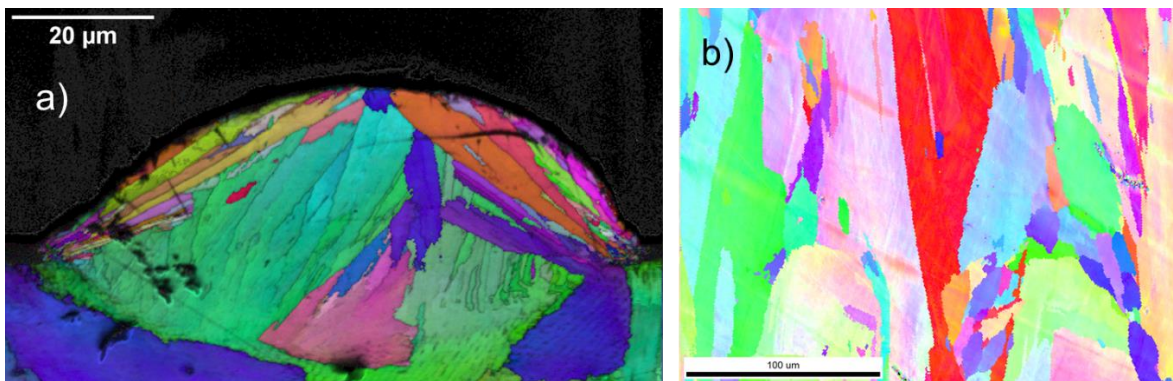


Figure 5-8. a) EBSD map of single track of IN718 printed using SLM process, b) EBSD map of IN718 sample printed using SLM process.

In AMD process, addition of the subsequent layers during printing process does not have any effect on the microstructure of lower layers as described in the earlier section. Hence, the thermal history related complications associated with SLM process are inherently absent for the AMD process.

5.4 CONCLUSION

Microstructure variation across the 3 layers of an AMD fabricated component was investigated using Electron Backscatter Diffraction (EBSD) analysis. No significant microstructure variation was observed in the 3 layers of the sample. Hence, by varying the acoustic energy density and strain rate during voxel deformation, microstructure of each

voxel can be manipulated thereby enabling the possibility of in-process microstructure control. The athermal process physics enables addition of material during fabrication without affecting the microstructure of the rest of the component, thus eliminating thermal history related complications which result in anisotropic microstructure in other heat energy based additive manufacturing processes like SLM.

CHAPTER 6

ANALYSIS OF ULTRASONIC ENERGY ASSISTED DIFFUSION

6.1 INTRODUCTION

As has been mentioned before, during the AMD process, ultrasonic energy enables bonding of a voxel of metal to the lower layer or the substrate. As the filament deforms from a circular cross-section to a rectangular cross-section, a simultaneous mass-transport across the filament-substrate or filament-lower layer interface allows for this bonding. The exact mechanism for this ultrasonic energy assisted mass transport and subsequent bonding has been a subject of debate in the literature.

In the literature on ultrasonic welding, a process in which sheets of metal are welded to each other using ultrasonic energy, the mass transport has been attributed to interfacial friction between the sheet and substrate. This friction results in a temperature rise. When welding Al6061 and Copper sheets, a temperature rise between 275 °C to 500 °C was observed [65]. During welding of 1060 Al alloy and T2 pure copper, the temperature was observed to be increasing by 125 °C for a welding time of 120 ms to about 350 °C for a welding time of 280 ms [66]. During ultrasonic spot welding of Al6111 sheets, a temperature rise of 350 °C was observed [67]. A similarly sharp but lesser temperature rise of around 200 °C was observed during the welding of Al6061 sheets [68]. A summary of interface weld temperatures measured with various techniques has been provided in [68]. Hu et. al observed very high diffusivity values during ultrasonic welding of copper foils. This observation was attributed to an increased vacancy concentration due to deformation

during the welding process [69]. It has been argued in the literature that the temperature values measured at the interface using thermocouples or IR imaging do not reflect the actual temperature values at the interface and that the actual values are much higher than the measured values. Regardless, in all the studies, the driver for mass transport across the interface has been the rapid temperature rise. The interfacial friction that causes the rapid temperature rise has also been observed to break the nascent oxide layers on the surfaces to bring metal surfaces in direct contact with each other. The other common feature of such ultrasonic welds are the intermetallic phases formed at the interface. For example, TiAl_3 phase was observed at the interface of Al5754-O and Ti-6Al-4V joints [70], CuAl_2 phase was observed at the interface of 6061 Al and pure copper [65] and FeAl_3 and Fe_2Al_5 phases were observed during welding of Al 6111-T4 to DC04 steel [71]. The formation of these stable equilibrium intermetallic phases is again attributed to the temperature driven diffusion and gradual decrease in the temperature due to dissipation of heat during which the evolution of these phases happens.

A very similar interfacial friction and temperature rise has been observed in ultrasonic consolidation. During ultrasonic consolidation of aluminum and copper, a temperature rise of around 465 °C was observed [72]. Based on the process parameter, the interface temperature measured using IR camera was found to vary from 75 °C to as high as 200 °C during ultrasonic consolidation of Al6061 alloy [73].

In contrast to this sharp temperature rise observed in ultrasonic welding and ultrasonic consolidation, in wire bonding, a temperature rise commensurate with the observed diffusion has not been recorded in the literature [74]. Mayer et al. used microsensors to measure the interface temperature during bonding of 25 μm , 60 μm and 75 μm gold wires.

The temperature rise was found to be ~ 10 °C [75]. Similarly, a negligible temperature rise was observed during ball bonding when the temperature was measured using thermopile temperature sensors [76]. To demonstrate that temperature rise is not a pre-requisite for ultrasonic bonding of wires, bonding of Al wires has been demonstrated in liquid nitrogen at a temperature of 77 K [77] [78].

The mechanics of AMD process are very similar to wire bonding. Indeed, using IR camera measurements, a temperature rise of ~ 5 °C was observed during deposition and bonding of a voxel of aluminum on aluminum substrate [18] [19]. In this chapter, using TEM analysis, the microstructure at the interface of Aluminum-Nickel bonds has been examined. Energy Dispersive Spectroscopy (EDS) analysis has been performed at the interface to quantify the diffusion and obtain diffusion profiles. Using Wagner's analysis, inter-diffusion coefficient for the Al-Ni material system has been calculated for a given ultrasonic energy density. This data combined with TEM microstructure analysis has been used to analyze the diffusion mechanism.

6.2 EXPERIMENTAL METHODS

The starting material used was a pure aluminum (99.99%) wire of 300 μm diameter. 3 separate voxels were deposited on a nickel substrate using the setup described in Chapter 2. Three different energy densities of 290 J/m^3 , 310 J/m^3 and 330 J/m^3 were used for each voxel respectively. A constant bond time of 450 ms was used for all 3 experiments.

6.2.1 SAMPLE PREPARATION FOR TEM

The 3 deposited voxels were cross-sectioned and polished using the same procedure as described in Chapter 3. Care was taken that all voxels are approximately polished up to the mid-plane of the voxel by putting an indent on the mid-plane before the sectioning and

polishing. A Focused Ion beam (FIB) was used to lift out a thin electron transparent lamella of the interface region between aluminum and nickel. Figure 6-1 shows the SEM images taken during the process. The process starts by depositing a protective platinum layer on the region of interest. Then, two trenches are milled on both sides of the region of interest. The lamella so formed is then welded to a needle and separated from the bulk of the material. This is followed by welding the lamella to TEM grid and then separating it from the needle. Further thinning is performed until the lamella is electron transparent.

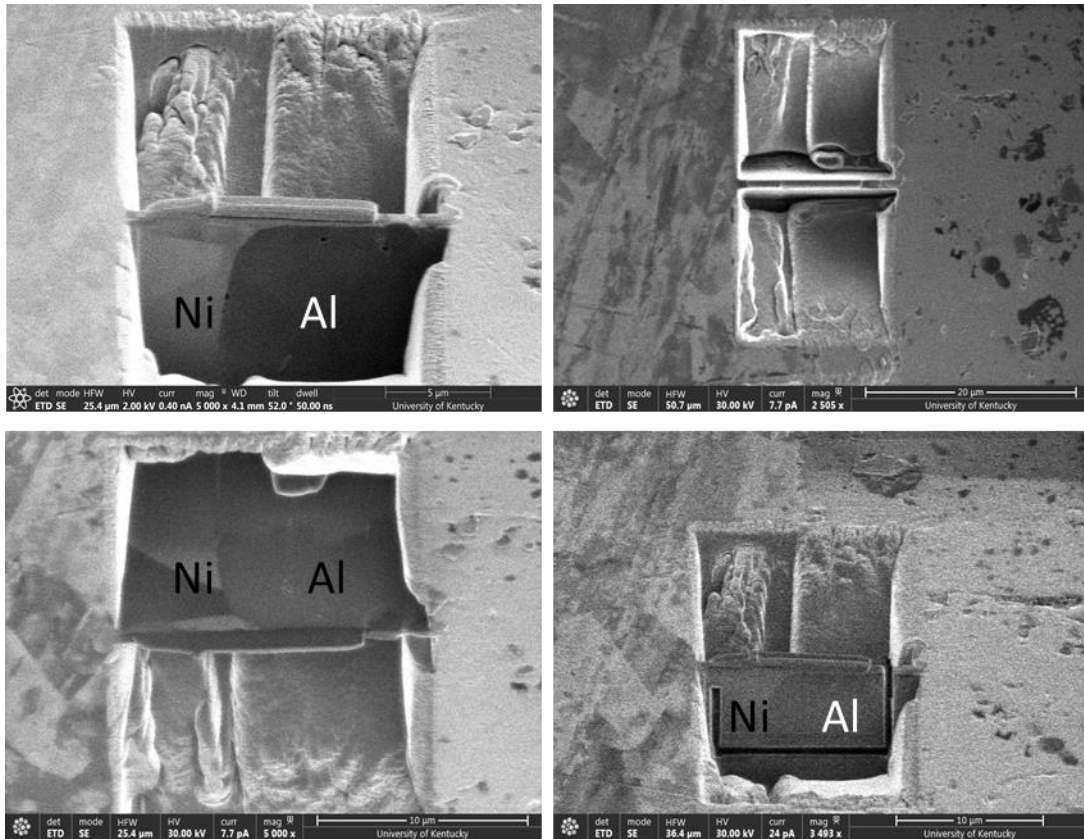


Figure 6-1. SEM images taken during the lift out of a thin electron transparent lamella of the Al-Ni interface region.

These electron transparent TEM lamellas/samples were analyzed in the Tecnai G2 F20 200kV TEM equipped with a EDAX EDS detector. High resolution TEM images and EDS line scans were captured.

6.3 RESULTS AND DISCUSSION

6.3.1 MICROSTRUCTURE AT THE INTERFACE

Figure 6-2 shows a TEM bright field image of the Al-Ni interface. In some regions of the interface, an amorphous region of aluminum oxide can be observed. This oxide is the native oxide on aluminum wire that gets trapped at some regions along the interface during the bonding process. To verify that the amorphous region at the interface is indeed aluminum oxide, an EDS map of the region was obtained. The map is shown in Figure 6-3. It is evident from the map that a region of the interface has excess concentration of oxygen indicating the presence of oxide in the region. Similar verification was also obtained from EDS quantification result shown in Table 6-1.

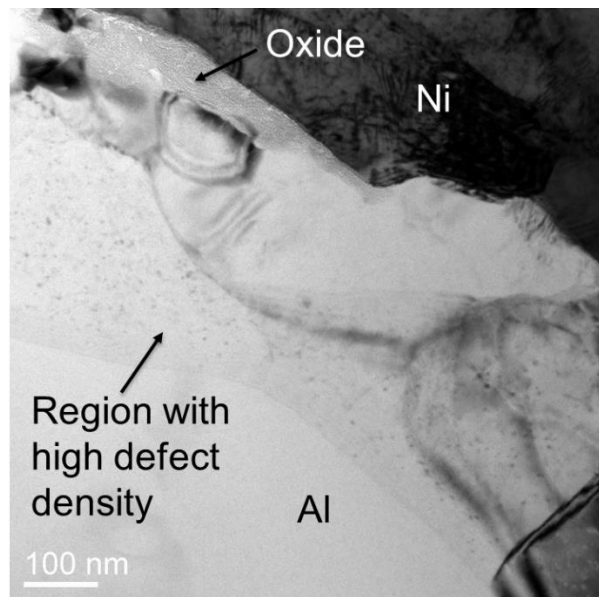


Figure 6-2. TEM bright field image of the Al-Ni interface.

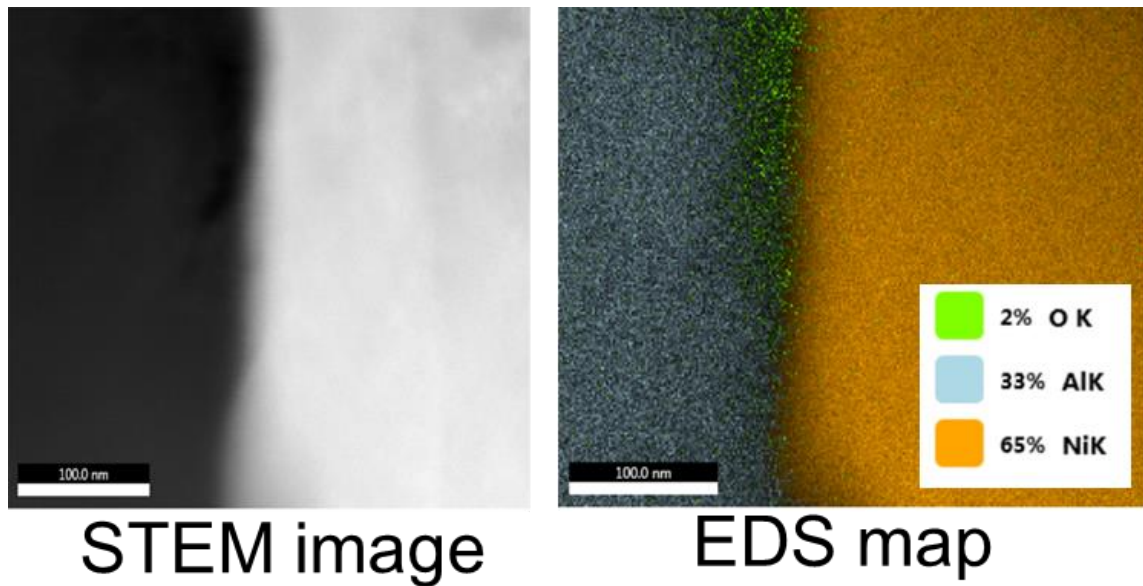


Figure 6-3. EDS map of the Al-Ni interface showing presence of oxygen content at the interface.

Table 6-1. EDS quantification result in the amorphous region at the Al-Ni interface.

Element	Weight %	Mole %	Error %	Net Int.	K Ratio	Z	A	F
Al 2O3	99.79	99.71	8.46	67.45	0.2257	0.9739	0.409	1.0004
Ni O	0.21	0.29	12.22	3.3	0.0025	0.9592	1.2473	1.1492

Figure 6-2 also shows a region on the aluminum side of the interface which has relatively high defect density. The region has been marked and labeled in the figure. A sharp transition between this region and the bulk of the deformed aluminum wire can be seen. In the region with high defect density, the grain size is of the order of ~10-100 nm. The effect of this high defect density in the deformed aluminum wire on the diffusion profile has been discussed in the next section. A high resolution TEM image of the region with high defect density taken along the [1 1 0] direction shows formation of stacking faults in the (1 1 1) planes. Such stacking faults have been observed in aluminum which has gone through

severe plastic deformation [79] [80]. This severe plastic deformation at the interface during deposition of Al voxels can be attributed to flow of the material in the lateral direction when the wire gets simultaneously deformed and to the flow of aluminum in the asperities on the substrate surface.

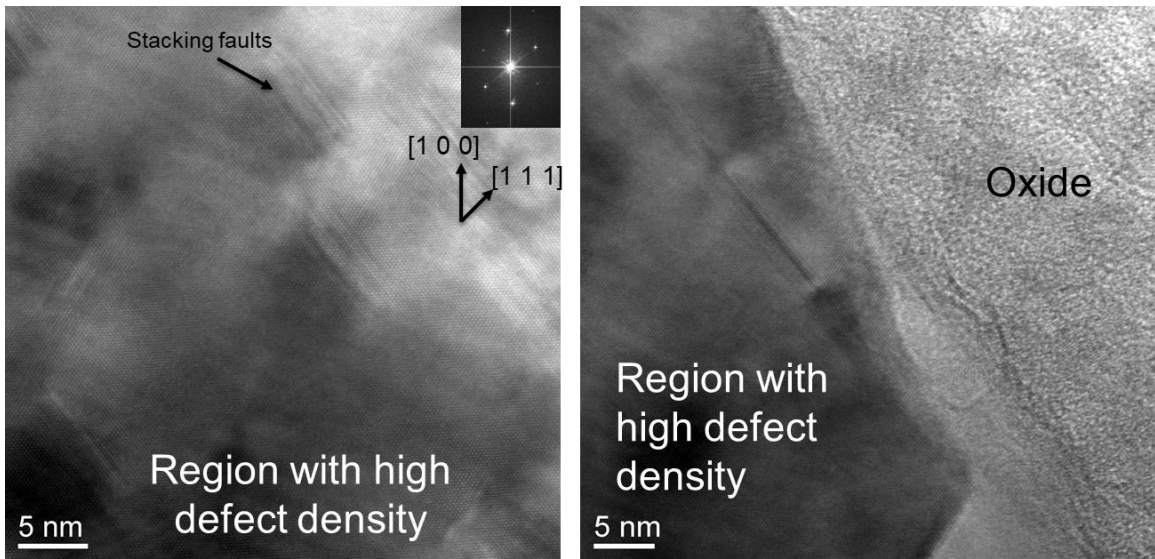


Figure 6-4. HRTEM image of the region with high defect density near the Al-Ni interface.

A high defect density region has also been observed at the interface of two materials during ultrasonic spot welding of aluminum sheets to copper substrates [81]. The formation of this region was attributed to interfacial friction in case of spot welding. This mechanism is different from the one observed during the bonding of wires where the interfacial friction stops after the first 20 milliseconds of the bonding process. The details of this have been given in the next section.

6.3.2 ANALYSIS OF DIFFUSION

Figure 6-5 shows the STEM image of the Al-Ni interface after bonding and the results of an EDS line scan which shows atomic percentage of each constituent versus distance after

smoothing the curves. 4 such EDS line scans were obtained at different locations on each of the 3 samples bonded using ultrasonic energy densities of 290 J/m³, 310 J/m³ and 330 J/m³. The resulting width of the inter diffusion zone was found to be ranging between ~80 nm to ~140 nm. Figure 6-6 summarizes the results. It is evident that the width of the inter-diffusion zone increases with an increase in the ultrasonic energy density.

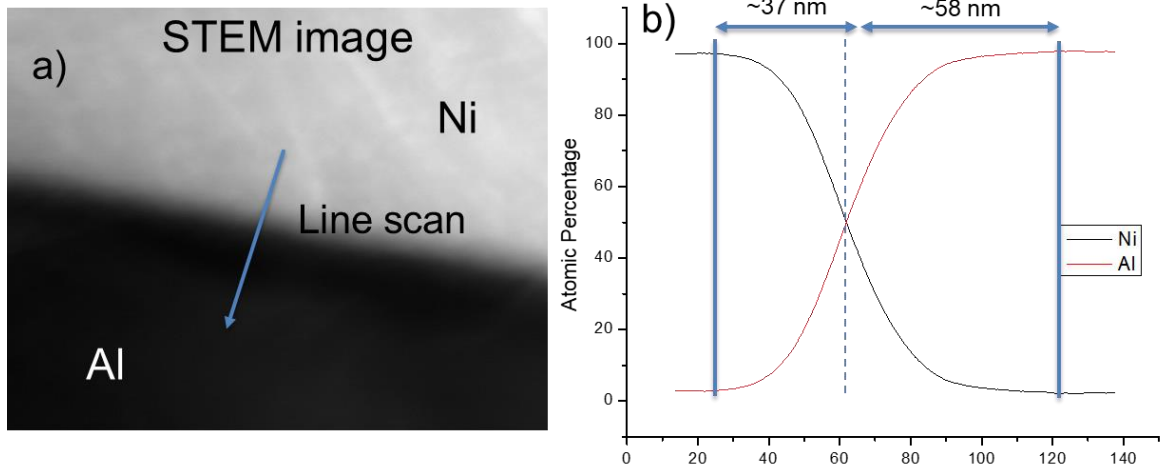


Figure 6-5. a) STEM of the bonded Al-Ni interface, b) Result of EDS line scan at the interface showing atomic percentage of each constituent versus distance.

A peculiar feature of the diffusion profile shown in Figure 6-5 is that the width of the inter-diffusion zone is larger on the aluminum side of the interface. This feature is consistent for all the diffusion profiles. This can be attributed to the region with high defect density observed in aluminum side. Higher defect density in this region leads to a more open aluminum lattice leading to increased diffusivity of nickel in aluminum. This increased defect density was also observed to assist in bond formation in ultrasonic welding where very high diffusivity of copper was observed in aluminum [69].

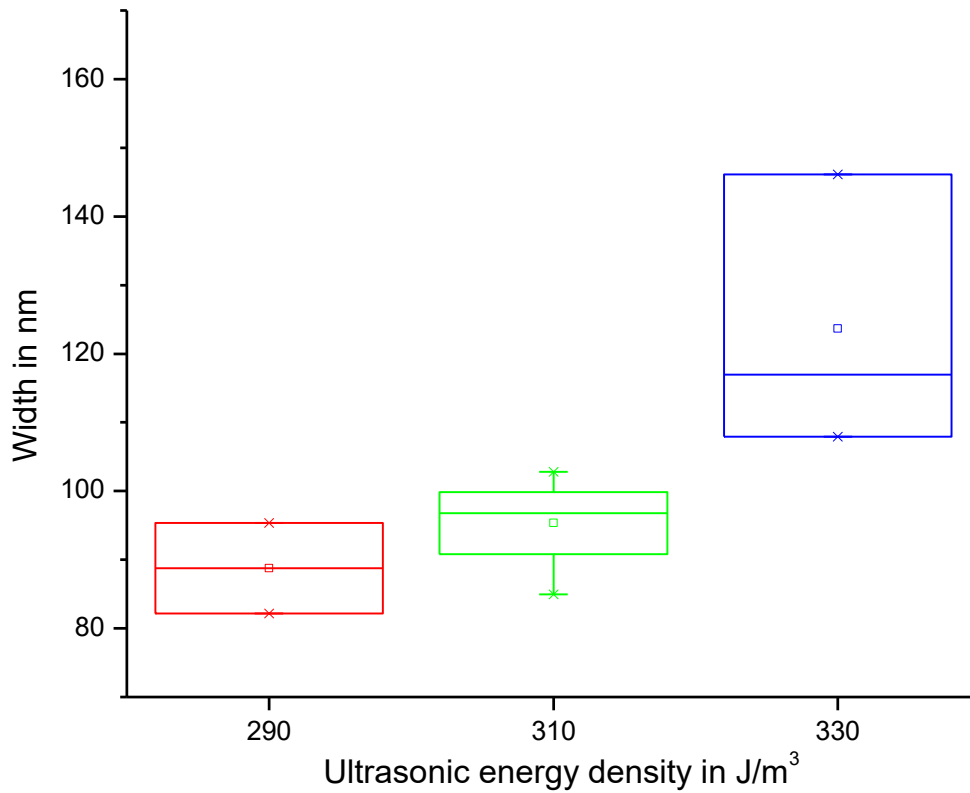


Figure 6-6. Graph showing the width of inter diffusion zone for different levels of ultrasonic energy densities.

6.3.3 ESTIMATION OF EFFECTIVE INTER-DIFFUSIVITY COEFFICIENT

The diffusion profile shown in Figure 6-5b was used to calculate the effective inter-diffusion coefficient of aluminum and nickel using Wagner's approach [82]. The objective of this analysis is to get an approximate value of the inter-diffusion coefficient. Hence, for simplicity, the assumption made is that the interface temperature remains constant throughout the bonding process.

According to Wagner's approach, the inter-diffusion coefficient is given by

$$\bar{D}(Y_B^*) = \frac{v_m^*}{2t(dY_B/dx)_x^*} \left[(1-Y_B^*) \int_{x^{-\infty}}^{x^*} \frac{Y_B}{v_m} dx + Y_B^* \int_{x^*}^{x^{\infty}} \frac{(1-Y_B)}{v_m} dx \right]$$

where,

x is the position along the curve,

v_m is the molar volume at composition of interest,

$$Y_B^* = \frac{N_B^+ - N_B^-}{N_B^+ - N_B^-}, N_B \text{ is the atomic fraction of nickel and } N_B^+ \text{ and } N_B^- \text{ are the nickel atomic}$$

fraction at the two extremes of the curve.

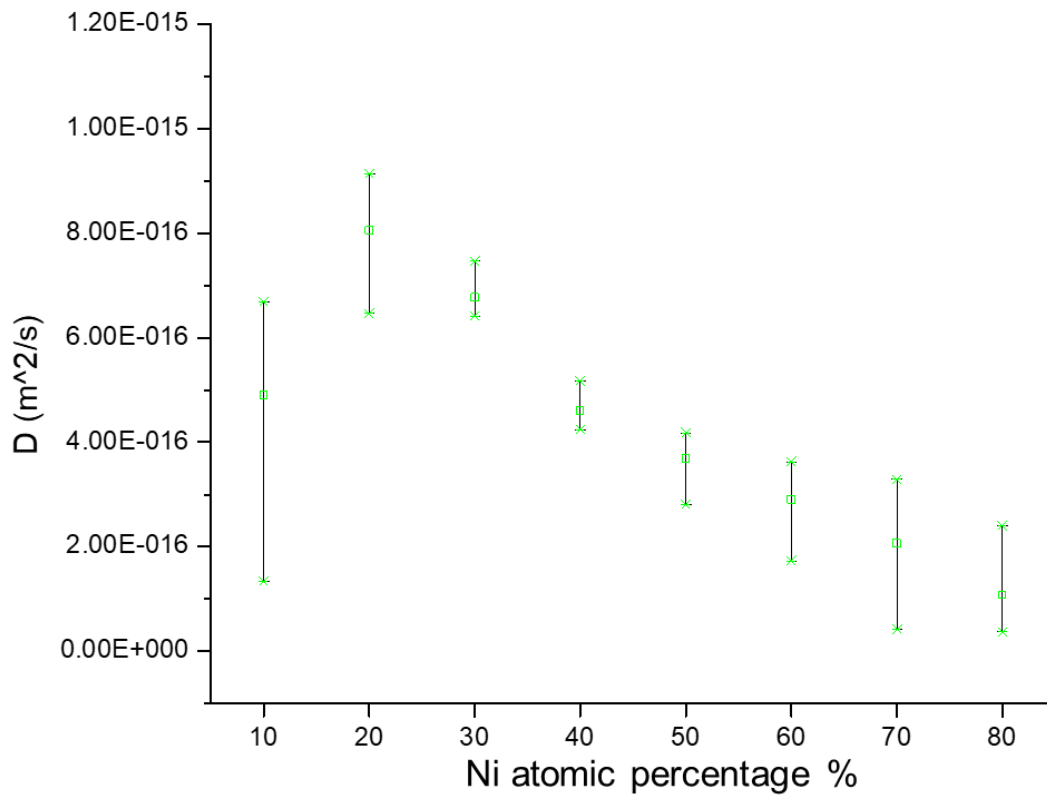


Figure 6-7. Graph of inter-diffusion coefficient between aluminum and nickel as a function of Ni atomic percentage for energy density of 310 J/m³.

Figure 6-7 shows the graph for of inter-diffusion coefficient between aluminum and nickel as a function of Ni atomic percentage for energy density of 310 J/m^3 . The values range from $\sim 1 \times 10^{-16} \text{ m}^2/\text{s}$ to $\sim 9 \times 10^{-16} \text{ m}^2/\text{s}$. By using the Arrhenius equation, $D = D_0 e^{-\frac{Q}{kT}}$ and using the values of D_0 and Q from the literature [83] [84], the effective constant temperature that would be required to achieve a diffusion zone of the size obtained in the experiments was calculated. The effective temperature values range from $\sim 320 \text{ }^\circ\text{C}$ to $420 \text{ }^\circ\text{C}$.

These temperatures values are much higher than the values from high speed infra-red camera measurements performed during the bonding process [18]. Figure 6-8 shows the results of the high-speed IR measurements. Figure 6-8a shows one frame of thermal video captured during bond formation showing the spatial temperature distribution in the vicinity of the interface at the time when the maximum temperature is reached. Presented in Figure 6-8b is the time evolution of the temperature at the filament-substrate interface. In Figure 6-8(b), the irradiation of ultrasonic vibrations start at the 50th millisecond. The relative movements between the two surfaces provide frictional heating that results in the sharp temperature rise. Another 30 milliseconds into the process, the metallurgical bond starts to form and the relative movements between the filament and substrate stops. This removes the frictional heat source and allows the interface temperature to drop. A maximum temperature rise of 5 degrees is observed. Another feature in the temporal temperature profile is the sharp reduction at 350 microseconds where the ultrasonic vibration stops. This indicates the removal of the second heat source in the process: cyclic plastic strain heating due to the high-frequency cyclic shear deformation in the voxel as it forms. Hence, the temperature rise during the process can be attributed to three heat sources as seen in the

temporal temperature evolution shown in Figure 6-8(b): (1) the volumetric heat generation from large amounts of plastic deformation associated with the height change in the filament during voxel formation, (2) the frictional heat generated due to the cyclic relative motion between the filament and the substrate that exists only during the initial ~20-30 ms, and (3) the cyclic shear deformation of voxel in the filament axial direction.

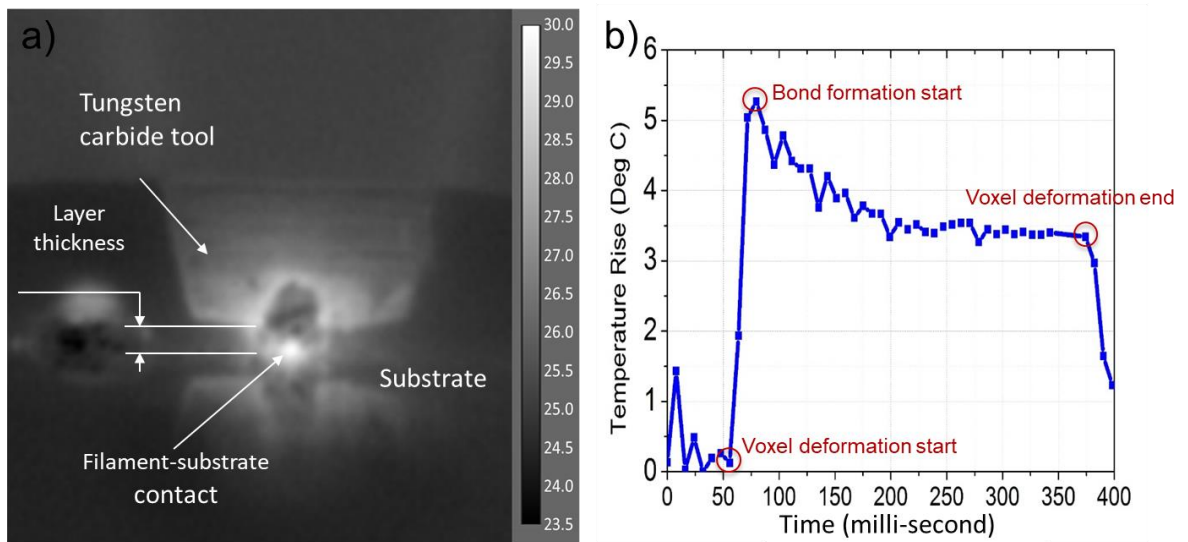


Figure 6-8. a) High speed IR camera snap shot of the instant at which maximum temperature rise is observed during the process, b) Temperature evolution at the interface versus time.

Another evidence for the temperature rise not being as high as that estimated from the inter-diffusion coefficient comes from the microstructure near the interface. In case of ultrasonic welding of aluminum and nickel where the measured (or estimated) temperature reached over 250 °C, formation of intermetallics was observed [85]. As mentioned in the Introduction section, such intermetallics at the interface are a common feature of ultrasonic welding and ultrasonic consolidation of dissimilar metals where the diffusion is driven by

interfacial friction and temperature rise. This temperature rise also drives the formation and growth of the intermetallics. But in the present work, where wires are bonded to the substrate, no such intermetallics have been observed as seen from the HRTEM image shown in Figure 6-9.

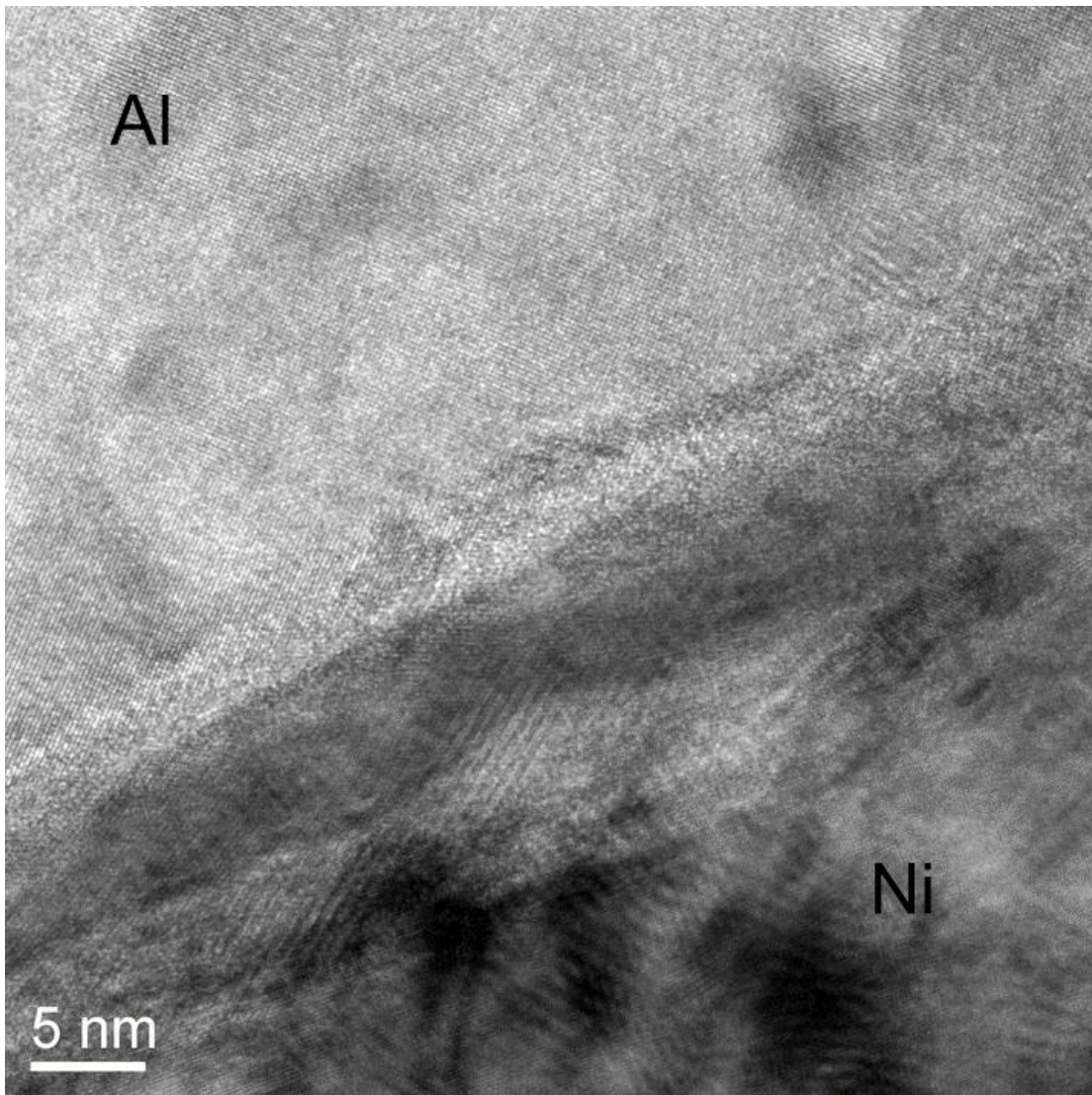


Figure 6-9. HRTEM image of the Al-Ni interface.

These two evidences distinguish the mechanism of voxel deposition during the AMD process from the mechanism of ultrasonic welding or ultrasonic consolidation. Hence, the

inter-diffusion of aluminum and nickel during the voxel deposition are not a temperature driven phenomenon. It is hypothesized that the irradiation of ultrasonic energy results in a rise in defect density (more specifically vacancies) in the metals. This defect density contributes to the annihilation of dislocations as observed in Chapter 3 due to increased frequency of dislocation climb. This increased defect density also contributes to the increased mass transport across the interface. To obtain a more direct evidence of this, in-situ measurements of the defect density during voxel deposition process will have to be performed.

6.4 CONCLUSION

A detailed analysis of the voxel bonding process has been presented in this chapter. Using TEM and EDS, the inter-diffusion of aluminum and nickel has been analyzed. Using the diffusion profiles obtained from EDS analysis, an approximate estimate of the inter-diffusion coefficient has been obtained. The amount of diffusion has been found to be much higher than that expected at the measured temperatures. HRTEM micrographs of the interface show an absence of intermetallics which would have otherwise formed in a process involving higher temperatures. The analysis distinguishes the mechanism of bond formation during the voxel deposition in AMD process with the mechanism of ultrasonic welding and ultrasonic consolidation.

CHAPTER 7

CONCLUSION AND FUTURE WORK

7.1 CONCLUSION

The dissertation addresses 2 key physical phenomenon of ultrasonic softening and ultrasonic energy assisted mass transport that govern the AMD process. The conclusions of this dissertation are summarized below:

- The dissertation demonstrates that AMD is a solid-state metal additive manufacturing process that is capable of fabricating near net-shape metal components in ambient condition. Ultrasonic/acoustic softening and ultrasonic energy assisted diffusion/mass transport are the two main phenomenon that govern the process. Being a solid-state process, it is also capable of printing multi-materials components with materials that have disparate melting temperatures.
- A one variable crystal plasticity model was modified to account for the acoustic softening to predict stress evolution during deposition of an aluminum voxel in the AMD process. From EBSD and TEM microstructure analysis, subgrain formation was observed during ultrasonic energy assisted deformation. It was also observed that ultrasonic energy assists in dislocation annihilation. This dislocation annihilation was accounted in the crystal plasticity model to predict stress evolution for deformation performed under the simultaneous application of ultrasonic energy with various energy density levels.
- The EBSD and TEM analysis was extended to copper and Al6061. The effect of stacking fault energy on the after-deformation microstructure was analyzed. It was observed that for copper, which is a medium stacking fault energy metal, lack of

dynamic recovery resulted in high dislocation density. Evidence of discontinuous dynamic recrystallization (DDR_X) was observed analogous to that in hot deformation. For Al6061, geometric dynamic recrystallization (gDR_X) was observed to be the recrystallization mechanism after ultrasonic energy assisted deformation.

- During the AMD process, the effect of adding subsequent layers of metal on the microstructure of the lower layers was analyzed using EBSD analysis. It was observed that the deposition of new layers does not have any effect on the microstructure of lower layers. This enables the prospect of individually controlling the microstructure of each voxel and thereby each layer being deposited during the AMD process. The microstructure evolution during the process was compared with SLM process in which the material has to go through a phase change and the repeated cyclic heating of the component results in epitaxial grain growth in the build direction, unlike in AMD process where the microstructure of the lower layers remains unaffected.
- To investigate the mechanism of bond formation during the deposition of the voxel in AMD process, high resolution TEM and EDS analysis was performed at the interface of aluminum voxels deposited on nickel substrates. A region of high defect density was observed on the aluminum side adjacent to the interface. The high defect density in this region enables more diffusion of nickel in aluminum which is evident from the diffusion profiles recorded using EDS analysis. Wagners method was used to calculate the effective inter-diffusion coefficient between aluminum and nickel. The values of inter-diffusion coefficient were found to be

much higher than those expected at the measured temperatures. The HRTEM analysis shows no formation of intermetallics distinguishing the process from ultrasonic welding and ultrasonic consolidation.

7.2 FUTURE WORK

The dissertation addresses key issues regarding the interaction of ultrasonic energy with metals, but it also opens scientific avenues that require further research and analysis, especially in the context of increasing the scope of AMD process and also the wide spread adoption of ultrasonic energy in manufacturing processes to take advantage of some of its characteristics listed in this dissertation. Some of these avenues are listed below-

- AMD process has been demonstrated for aluminum, gold, copper aluminum alloys like Al6061. Process parameters need to be developed to bring more materials in the purview of the process.
- The dissertation presents a detailed analysis of the microstructure evolution during ultrasonic assisted deformation of FCC metals. A similar understanding of microstructure evolution for metals with other crystal structure need to be undertaken. This fundamental understanding will help in predicting post processing microstructure of these metals.
- It has been hypothesized that the ultrasonic softening and increased mass transport are due to increased defect density during ultrasonic irradiation. The dissertation provides indirect evidence for this hypothesis, but further analysis is required to obtain direct evidence of the hypothesis. In-situ defect density measurements during irradiation of ultrasound on metals need to be performed. Some measurements techniques include resistivity measurement to obtain an indirect

evidence of the change in defect density and positron annihilation method. These experiments will be able to address the fundamental mechanism of defect evolution during the process.

REFERENCES

- [1] D. L. Bourell, M. C. Leu and D. W. Rosen, "Roadmap for Additive Manufacturing Identifying the Future of Freeform Processing," in *International Solid Freeform Fabrication Symposium*, Austin, Texas, 2009.
- [2] J. Stansbury and M. Idacavage, "3D printing with polymers: Challenges among expanding options and opportunities," *Dental Materials*, vol. 32, no. 1, pp. 54-64, 2016.
- [3] D. D. Gu, W. Meiners, K. Wissenbach and R. Poprawe, "Laser additive manufacturing of metallic components: materials, processes and mechanisms," *International Materials Reviews*, vol. 57, no. 3, pp. 133-164, 2012.
- [4] I. Wolff, "Breathing Safely Around Metal 3D Printers," *Manufacturing Engineering*, 2016.
- [5] N. Guo and M. C. Leu, "Additive Manufacturing: technology, applications and research needs," *Front. Mech. Eng.*, vol. 8, no. 3, pp. 215-243, 2013.
- [6] D. White, "ULtrasonic Consolidation of aluminum tooling," *advanced materials and processes*, vol. 161, pp. 64-65, 2003.
- [7] G. Ram, C. Robinson, Y. Yang and B. Stucker, "Use of Ultrasonic Consolidation for Fabrication of Multi-Material Structures," *Rapid Prototyping Journal*, vol. 13, no. 4, pp. 226-235, 2007.
- [8] M. Sriraman, M. Gonser, H. Fujii, M. Bloss and S. Babu, "Thermal transients during processing of materials by very high power ultrasonic additive manufacturing," *Journal of Materials Processing Technology*, vol. 211, pp. 1650-1657, 2011.
- [9] A. B. Spierings, N. Herres and G. Levy, "Influence of the particle size distribution on surface quality and mechanical properties in AM steel parts," *Rapid Prototyping Journal*, vol. 17, no. 3, pp. 195-202, 2011.
- [10] D. Thomas and S. Gilbert, "Costs and Cost Effectiveness of Additive Manufacturing," NIST Special Publication 1176, 2014.
- [11] J. Hu and M.-F. Yu, "Meniscus-confined three-dimensional electrodeposition for direct writing of wire bonds," *Science*, vol. 329, no. 16, pp. 313-316, 2010.
- [12] D. Semenok, "LCLD Laser processing technology for microelectronics printed circuit boards of new generation," *Proceedings of the 7th international conference interdisciplinarity in engineering*, vol. 12, pp. 277-282, 2014.

- [13] V. A. Kochemirovsky, S. Fateev, L. Logunov, I. Tumkin and S. Safonov, "Laser-Induced Copper Deposition with Weak Reducing Agents," *Int. J. Electrochem. Sci.*, vol. 9, pp. 644-658, 2014.
- [14] G. Anzalone, C. Zhang, B. Wijnen, P. Sanders and J. Pearce, "A low-cost open-source metal 3D printer," *IEEE Access*, vol. 1, pp. 803-810, 2013.
- [15] A. Haselhuhn, B. Wijnen, G. Anzalone, P. Sanders and J. Pearce, "In situ formation of substrate release mechanisms for gas metal arc weld metal 3D printing," *Journal of Materials Processing Technology*, vol. 226, pp. 50-59, 2015.
- [16] A. Haselhuhn, M. Buhr, B. Wijnen, P. Sanders and J. Pearce, "Structure-property relationships of common aluminum weld alloys utilized as feedstock for GMAW-based 3D metal printing," *Materials Science & Engineering A*, vol. 673, pp. 511-523, 2016.
- [17] U. Geibler, M. Schneider-Ramelow, K.-D. Lang and H. Reichl, "Investigation of microstructural processes during ultrasonic wedge/wedge bonding of AlSi1 wires," *Journal of Electronic Materials*, vol. 35, no. 1, 2006.
- [18] A. Deshpande and K. Hsu, "Acoustoplastic Metal Direct-write: Towards Solid Aluminum 3D Printing in Ambient Conditions," *Additive Manufacturing*, vol. 19, pp. 73-80, 2018.
- [19] A. Deshpande, "A Study on the Use of Kilohertz Acoustic Energy for Aluminum Shaping and Mass Transport in Ambient Condition Metal 3D Printing," Arizona State University, Ann Arbor, 2016.
- [20] M. L. J.-M. K. D.-W. K. C. W. Hongjun Ji, "Nano features of Al/Au ultrasonic bond interface observed by high resolution transmission electron microscopy," *Materials Characterization*, vol. 59, pp. 1419-1424, 2008.
- [21] B. Langenecker, "Effects of Ultrasound on Deformation Characteristics," *IEEE Transaction of sonics and ultrasonics*, Vols. SU-13, no. 1, March 1966.
- [22] J. A. George G. Harman, "The Ultrasonic Welding Mechanism as Applied to Al-Au wire bonding," *IEEE Transaction on parts*, Vols. PHP-13, no. 1, December 1977.
- [23] C. Yang, X. Shan and T. Xie, "Titanium wire drawing with longitudinal-torsional composite ultrasonic vibration," *International Journal of Advanced Manufacturing Technology*, vol. 83, pp. 645-655, 2016.
- [24] A. Abdullah, M. Paknejad, S. Dashti, A. Pak and A. M. Beigi, "Theoretical and experimental analyses of ultrasonic-assisted indentation forming of tube," *Journal of Engineering Manufacture*, vol. 228, no. 3, pp. 388-398, 2014.

- [25] S. Amini, A. H. Gollo and H. Paktinat, "An investigation of conventional and ultrasonic-assisted forming of annealed AA1050 sheet," *International Journal of Advanced Manufacturing Technology*, 2016.
- [26] Y. B. Zhong, C. S. Wu and G. K. Padhy, "Effect of ultrasonic vibration on welding load, temperature and material flow in friction stir welding," *Journal of Materials Processing Technology*, vol. 239, pp. 273-283, 2017.
- [27] W. F. L. H. J. Z. Junhui Lei, "Theoretical and experimental analyses of atom diffusion characteristics on wire bonding," *JOURNAL OF PHYSICS D: APPLIED PHYSICS*, vol. 41, 2008.
- [28] M. L. J.-M. K. D.-W. K. C. W. Hongjun Ji, "Nano features of Al/Au ultrasonic bond interface observed by high resolution electron microscopy," *Materials Characterization*, vol. 59, pp. 1419-1424, 2008.
- [29] A. Rusinko, "Analytical description of ultrasonic hardening and softening," *Ultrasonics*, vol. 51, pp. 709-714, 2011.
- [30] E. S. Amir Siddiq, "Ultrasonic-assisted manufacturing processes: Variational model and numerical simulations," *Ultrasonics*, vol. 52, pp. 521-529, 2012.
- [31] G.-Y. K. Z. W. L. F. Q. Z. D. M. Z. C. Zhehe Yao, "Acoustic softening and residual hardening in aluminum: Modeling and experiments," *International Journal of Plasticity*, vol. 39, pp. 75-87, 2012.
- [32] T. Sakai, A. Belyakov, R. Kaibyshev, H. Miura and J. J. Jonas, "Dynamic and post-dynamic recrystallization under hot, cold and severe plastic deformation conditions," *Progress in Material Science*, vol. 60, pp. 130-207, October 2013.
- [33] H.J.McQueen, "Elevated temperature deformation at Forming rates of 10^{-2} to 10^2 s^{-1} ," *Mettallurgical and material transactions*, vol. 33A, pp. 347-362, February 2002.
- [34] H. J. McQueen and W. Blum, "Dynamic recovery: sufficient mechanism in the hot deformation of Al (<99.99)," *Material Science & Engineering A*, vol. 290, pp. 95-107, 2000.
- [35] Y. Estrin, "Dislocation-density-related constitutive modeling," in *Unified constitutive laws of plastic deformation*, San Diego, Academic Press, 1996, pp. 69-106.
- [36] H. J. Frost and M. F. Ashby, *Deformation-mechanism maps: The plasticity and creep of metals and ceramics*, New York: Pergamon Press, 1982.
- [37] U. F. Kocks, "Constitutive behavior based on crystal plasticity," in *Unified Constitutive equations for creep and plasticity*, A. K. Miller, Ed., London, Elsevier, 1987, pp. 1-88.

- [38] U. F. Kocks, "Laws for work-hardening and low temperature creep," *Journal of Engineering Manufacturing and Technology*, vol. 98, pp. 76-85, 1976.
- [39] H. Mecking and U. F. Kocks, "Kinetics of flow and strain-hardening," *Acta Metallurgica*, vol. 29, pp. 1865-1875, 1981.
- [40] Y. Estrin, "Dislocation theory based constitutive modelling: foundations and application," *Materials Processing Technology*, pp. 33-39, 1998.
- [41] Y. Estrin, "Constitutive modelling of creep of metallic materials: Some simple recipes," *Material Science & Engineering A*, vol. 463, pp. 171-176, 2007.
- [42] H. J. McQueen and K. Conrad, "Recovery and recrystallization in the hot-working of aluminum alloys," in *Microstructural control in aluminum alloys: Deformation, recovery and recrystallization*, E. H. Chia and H. J. McQueen, Eds., New York, The Metallurgical society, 1985, pp. 197-219.
- [43] U. F. Kocks and H. Mecking, "Physics and phenomenology of strain hardening: the FCC case," *Progress in material science*, vol. 48, pp. 171-273, 2003.
- [44] W. D. Callister Jr., *Material Science and Engineering an introduction*, John Wiley & sons, Inc, 2007.
- [45] K. W. Siu, A. H. W. Ngan and I. P. Jones, "New insight on acoustoplasticity – Ultrasonic irradiation enhances subgrain formation during deformation," *International journal on plasticity*, vol. 27, pp. 788-800, 2011.
- [46] K. H. Westmacott and B. Langenecker, "Dislocation structure in ultrasonically irradiated aluminum," *Physical review letters*, vol. 14, no. 7, pp. 221-224, 1965.
- [47] E. G. Amir Siddiq, "Thermomechanical analyses of ultrasonic welding process using thermal and acoustic softening," *Mechanics of Materials*, vol. 40, pp. 982-1000, 2008.
- [48] E. Mariani and E. Ghassemieh, "Microstructure evolution of 6061 O Al alloy during ultrasonic consolidation: An insight form electron backscatter diffraction," *Acta Materialia*, vol. 58, pp. 2492-2503, 2009.
- [49] H. Peng, D. Chen and X. Jiang, "Microstructure and mechanical properties of an ultrasonic spot welded aluminum alloy: The effect of welding energy," *Materials*, vol. 10, pp. 449-464, 2017.
- [50] H. Zhou, H. Cui, Q.-H. Qin, H. Wang and Y. Shen, "A comparative study of mechanical and microstructural characteristics of aluminium and titanium undergoing ultrasonic assisted compression testing," *Materials Science & Engineering A*, vol. 682, pp. 376-388, 2017.

- [51] K. Huang and R. E. Loge, "A review of dynamic recrystallization phenomena in metallic materials," *Materials and Design*, vol. 111, pp. 548-574, 2016.
- [52] W. Blum, Q. Zhu, R. Merkel and H. J. McQueen, "Geometric dynamic recrystallization in hot torsion of Al-5Mg-0.6Mn," *Materials Science & Engineering A*, vol. 205, pp. 23-30, 1996.
- [53] A. Hadadzadeh, F. Mokdad, M. A. Wells and D. L. Chen, "A new grain orientation spread approach to analyze the dynamic recrystallization behavior of a cast-homogenized Mg-Zn-Zr alloy using electron backscatter diffraction," *Materials Science & Engineering A*, vol. 709, pp. 285-289, 2018.
- [54] A. M. Wusatowska-Sarnek, "The new grain formation during warm and hot deformation of copper," *Journal of Engineering Materials and Technology*, vol. 127, pp. 295-300, 2005.
- [55] H. J. McQueen and C. A. C. Imbert, "Dynamic recrystallisation: plasticity enhancing structural development," *Journal of alloys and compounds*, vol. 378, pp. 35-43, 2004.
- [56] H. J. McQueen, S. Spigarelli, M. E. Kassner and E. Evangelista, *Hot Deformation and Processing of Aluminum Alloys*, CRC press, 2011.
- [57] W. H. Van Geertruyden, W. Z. Misiolek and P. T. Wang, "Grain structure in a 6061 aluminum alloy during torsion," *Materials Science & Engineering A*, vol. 419, pp. 105-114, 2006.
- [58] H. J. McQueen and I. Poschmann, "Subgrain development in hot working of Al and Al-5Mg," *Materials Science & Engineering A*, vol. 1997, pp. 830-833, 1997.
- [59] A. Deshpande and K. Hsu, "Acoustic energy enabled dynamic recovery in aluminium and its effects on stress evolution and post-deformation microstructure," *Materials Science & Engineering A*, vol. 711, pp. 62-68, 2018.
- [60] C. Li, R. White, X. Y. Fang, M. Weaver and Y. B. Gui, "Microstructure evolution characteristics of Inconel 625 alloy from selective laser melting to heat treatment," *Material Science and Engineering A*, vol. 705, pp. 20-31, 2017.
- [61] D. Tomus, Y. Tian, P. A. Romtesch, M. Heilmaier and X. Wu, "Influence of post heat treatments on anisotropy of mechanical behavior and microstructure of Hastelloy-X parts produced by selective laser melting," *Material Science and Engineering A*, vol. 667, pp. 42-53, 2016.
- [62] J. Gockel and J. Beuth, "Understanding Ti-6Al-4V Microstructure Control in Additive Manufacturing via process maps," in *28th Annual International Solid Freeform Fabrication (SFF) Symposium*, Austin, texas, 2017.
- [63] S. Raghavan, Z. Baicheng, P. Wang, C.-N. Sun, M. L. Sharon, T. Li and J. Wei, "Effect of different heat treatments on the microstructure and mechanical properties

- in selective laser melted Inconel 718 alloy," *Materials and Manufacturing Processes*, 2016.
- [64] K. Kempen, L. Thijs, J. V. Humbeeck and J. P. Kruth, "Mechanical properties of AlSi10Mg produced by selective laser melting," *Physics Procedia*, vol. 39, pp. 439-446, 2012.
- [65] J. W. Yang, B. Cao, X. C. He and H. S. Luo, "Microstructure evolution and mechanical properties of Cu-Al joints by ultrasonic welding," *Science and Technology of welding and joining*, vol. 19, no. 6, pp. 500-504, 2014.
- [66] G. Liu, X. Hu, Y. Fu and Y. Li, "Microstructure and mechanical properties of ultrasonic welded joint of 1060 Aluminum alloy and T2 pure copper," *Metals*, vol. 7, pp. 361-371, 2017.
- [67] D. Bakavos and P. B. Prangnell, "Mechanisms of joint and microstructure formation in high power ultrasonic spot welding 6111 aluminium automotive sheet," *Materials Science and Engineering A*, vol. 527, pp. 6320-6334, 2010.
- [68] E. de Vries, *Mechanics and mechanisms of ultrasonic metals welding*, Ohio State University, 2004.
- [69] T. Hu, S. Zhalehpour, A. Gouldstone, S. Muftu and T. Ando, "A method for the estimation of the interface temperature in ultrasonic joining," *Metallurgical and Materials Transactions A*, vol. 45, no. A, pp. 2545-2552, 2014.
- [70] S. Q. Wang, V. K. Patel, S. D. Bhole, G. D. Wen and D. L. Chen, "Microstructure and mechanical properties of ultrasonic spot welded Al/Ti alloy joints," *Materials and Design*, vol. 78, pp. 33-41, 2015.
- [71] F. Haddadi, "Rapid intermetallic growth under high strain rate deformation during high power ultrasonic spot welding of aluminium to steel," *Materials and Design*, vol. 66, pp. 459-472, 2015.
- [72] J. Sietins, J. Gillespie and S. Advani, "Transmission electron microscopy of an ultrasonically consolidated copper-aluminum interface," *Journal of Materials Research*, vol. 29, no. 17, pp. 1970-1977, 2014.
- [73] S. Koellhoffer, J. W. Gillespie Jr., S. G. Advani and T. A. Bogetti, "Role of friction on the thermal development in ultrasonically consolidated aluminum foils and composites," *Journal of Materials Processing Technology*, vol. 211, pp. 1864-1877, 2011.
- [74] G. Harman, *Wire bonding in microelectronics*, McGraw Hill, 2010.
- [75] M. Mayer, O. Paul and H. Baltes, "In-situ measurement of stress and temperature under bonding pads during wire bonding using integrated sensors," in *Proceeding of 2nd international conference on emerging electronics*, Bangalore, 1998.

- [76] S. Suman, M. Gaitan, Y. Joshi and G. G. Harman, "Wire-Bonding Process Monitoring Using Thermopile temperature sensors," *IEEE transactions on advanced packaging*, vol. 28, no. 4, pp. 685-693, 2005.
- [77] K. C. Joshi, "The formation of ultrasonic bonds," *Welding Journal*, pp. 840-848, December 1971.
- [78] G. Harman and K. O. Leedy, "An experimental model of the microelectronic ultrasonic wire bonding mechanism," in *10th Annual Proc. Reliability Physics*, Las Vegas, 1972.
- [79] W. Z. Han, G. M. Cheng, S. X. Li, S. D. Wu and Z. F. Zhang, "Deformation induced microtwins and stacking faults in aluminum single crystals," *Physical review letters*, vol. 101, 2008.
- [80] M. Kiritani, "Story of stacking faults tetrahedra," *Materials chemistry and physics*, vol. 50, pp. 133-138, 1997.
- [81] Z. Zhang, K. Wang, J. Li, Q. C. Yu and W. Cai, "Investigation of interfacial layer for ultrasonic spot welded aluminum and copper joints," *Scientific Reports*, vol. 7, 2017.
- [82] A. Paul, T. Laurila, V. Vuorinen and S. V. Divinski, *Thermodynamics, diffusion and the Kirkandall effect in solids*, Springer, 2014.
- [83] A. Paul, A. A. Kodentsov and F. J. J. van Loo, "On diffusion in beta-NiAl phase," *Journal of alloys and compounds*, vol. 403, pp. 147-153, 2005.
- [84] A. Green and N. Swindells, "Measurement of interdiffusion coefficients in Co-Al and Ni-Al systems between 1000 and 1200 deg C," *Materials Science and Technology*, vol. 1, pp. 101-103, 1985.
- [85] Z. L. Ni and F. X. Ye, "Weldability and mechanical properties of ultrasonic welded aluminum and nickel joints," *Materials letters*, vol. 185, pp. 204-207, 2016.

CURRICULUM VITAE

Name: Anagh T. Deshpande
Email: anagh.deshpande@gmail.com, Cell: 480-330-9518
Address: 2204 James Pirtle Ct, Apt. 3, Louisville, KY- 40217

EDUCATION

- | | |
|---|----------------------------|
| University of Louisville, J. B. Speed School of Engineering
PhD in Mechanical Engineering, GPA-4
Research Adviser: Dr. Keng Hsu | Louisville, KY
Feb 2019 |
| Arizona State University, Ira A. Fulton Schools of Engineering
MS in Manufacturing Engineering, GPA-4
Research Adviser: Dr. Keng Hsu | Tempe, Arizona
May 2016 |
| University of Mumbai, Fr. C. Rodrigues Institute of Technology
BE in Mechanical Engineering | Mumbai, India
May 2012 |

JOURNAL PUBLICATIONS

- **Deshpande, A.**, Nath, S. D., Fernandez, E., Atre, S. & Hsu, K., Microstructure and mechanical property characterization of Ni-based superalloy Haynes-282 fabricated using Selective Laser Melting (SLM), Under preparation.
- **Deshpande, A.** & Hsu, K., Microstructure evolution of Al6061 and copper during ultrasonic energy assisted deformation, Materials Characterization, Under review.
- **Deshpande, A.**, Ravi, A. K., Kusel, S., Churchwell, R. & Hsu, K., Interlayer thermal history modification for interface strength in fused filament fabricated parts, Progress in Additive Manufacturing (2018).
- **Deshpande, A.** & Hsu, K., 2018. Acoustic energy enabled dynamic recovery in aluminium and its effects on stress evolution and post-deformation microstructure. Materials Science & Engineering A, Volume 711, pp. 62-68.
- **Deshpande, A.** & Hsu, K., 2018. Acoustoplastic metal direct-write: Towards solid aluminum 3D printing in ambient conditions. Additive Manufacturing, Volume 19, pp. 73-80.
- Ravi, A. K., **Deshpande, A.** & Hsu, K., An in-process laser localized pre-deposition heating approach to inter-layer bond strengthening in extrusion based polymer additive manufacturing. Journal of Manufacturing Processes, Volume 24, pp. 179-185.

PATENTS

- Keng Hsu and **Anagh Deshpande**, “Systems and methods for additive manufacturing utilizing localized ultrasound-enhanced material flow and fusion” (2015), US Provisional Patent 62/210,041, US Utility patent pending.
- Keng Hsu and **Anagh Deshpande**, “Acoustic-energy based material deposition and repair”, US Utility patent pending.

CONFERENCE PROCEEDINGS AND PRESENTATIONS

- **Anagh Deshpande** and Keng Hsu, “Microstructure evolution during solid-state ambient condition metal additive manufacturing”, Solid Freeform Fabrication (SFF) 2018.
- **Anagh Deshpande** and Keng Hsu, “Microstructure characterization of as-printed Ni-based superalloys fabricated using Laser Powder Bed Fusion process”, Additive Manufacturing with Powder Metallurgy (AMPM) 2018.
- **Anagh Deshpande** and Keng Hsu, “Ultrasonic energy enabled dynamic recovery in aluminium during micro forming and its effects on stress and microstructure evolution”, Material Science and Technology (MS&T) 2017.
- **Anagh Deshpande** and Keng Hsu, “Acoustic energy based additive manufacturing of fully dense parts at room temperature and in-process tailoring of the microstructure”, AeroDef 2017.
- **Anagh Deshpande** and Keng Hsu, “Ultrasonic Filament Modeling: Metal Additive Manufacturing of Fully Dense Parts at Room Temperature”, RAPID 2016.

ACADEMIC EXPERIENCE

University of Louisville, J. B. Speed School of Engineering

Louisville, KY

Teaching Assistant

- ME 521: Mechanical Vibrations Fall 2017
- ME 381: Introduction to Manufacturing Spring 2018
- ME 435: Systems Dynamics Summer 2018

INDUSTRY EXPERIENCE

Godrej & Boyce Private Limited, Godrej Precision Systems Division

Mumbai, India

Assistant Manager

Aug 2012-July 2014

- Developed manufacturing processes for new products.
- Supervised welding activity, NDTs (Non-destructive tests) to identify weld defects and repair of the defects. Performed pressure-test (hydro), leak-test (pneumo) and flow tests on all hardware. Ensured all the hardware meet the stringent quality standards.
- Performed production planning of CNC and conventional machines and man-power management of 40 workmen.
- Analyzed production and delivery data to determine potential improvement areas. Carried out continuous improvement (Kaizen) activities which resulted in financial saving, improved productivity and safety.

AWARDS

- National Science Foundation Grant to attend Solid Freeform Fabrication (SFF) conference, 2018
- National Science Foundation grant to attend AMPM conference, 2018
- Best research presentation award by ASME UofL chapter, 2018
- Best poster award at AeroDef conference, 2017
- Society of Manufacturing Engineers (SME) travel grant to attend AeroDef conference, 2017
- Lean Six Sigma Black Belt
- Membership of collegiate honor society Phi kappa Phi
- Membership of engineering honor society Tau Beta Pi

SKILLS

- Advanced material characterization: TEM, FIB, SEM, AFM, XRD, EDS, EBSD.
- Hands on: Metal additive manufacturing equipment (Concept laser and EOS equipment), CNC and manual milling and lathe machines, furnaces and ovens, DIC technique for strain analysis.

- Finite element analysis/CAD: Ansys, SolidWorks, AutoCAD.
- Software: MS Excel, MS PowerPoint, Origin.
- Coding: Matlab, C++.